

Exogeological inferences from white dwarf pollutants: the impact of stellar physics

Andrew M. Buchan¹*, Pier-Emmanuel Tremblay¹, Antoine Bédard¹, Evan B. Bauer^{2,3}
and Tim Cunningham³

¹Department of Physics, University of Warwick, Coventry CV4 7AL, UK

²Lawrence Livermore National Laboratory, Livermore, CA 94550, USA

³Center for Astrophysics, Harvard & Smithsonian, 60 Garden Street, Cambridge, MA 02138, USA

arXiv:2510.17985v1 [astro-ph.EP] 20 Oct 2025

Accepted XXX. Received YYY; in original form ZZZ

ABSTRACT

Many white dwarfs have accreted material from their own planetary systems. These objects can be used to infer the composition of exoplanetary material and identify evidence for key geological processes. However, the white dwarf atmospheric physics distorts the inferred material composition away from the true composition, mainly through differential atomic diffusion of the accreted metals. Correcting for this effect is essential, but is dependent on various physical assumptions associated with the white dwarf itself. We first focus on the effect of assumptions related to convective overshoot and thermohaline mixing on the atomic diffusion timescales. For white dwarfs with H-dominated atmospheres between 12 000 K and 18 000 K, we find that including a complete treatment of convective overshoot decreases the inferred Fe and O abundances in accreted material. For these white dwarfs, we also find that including thermohaline mixing decreases Fe and O abundances. For He-dominated systems, the effect of convective overshoot is comparatively minor. We then explore the overall effect of other physical assumptions by comparing publicly available grids of diffusion timescales. We find that the choice of model grid can have a large impact for white dwarfs with He-dominated atmospheres, notably on the inferred core to mantle ratio of accreted material. We identify several systems for which the geological interpretation is robust against these systematics. We also present a ‘discrepancy metric’ which can be used to estimate the potential impact of changing the stellar physics without requiring detailed modelling.

Key words: planets and satellites: composition – planets and satellites: physical evolution – stars: atmospheres – stars: fundamental parameters – white dwarfs

1 INTRODUCTION

White dwarfs, the remnants of main sequence stars with masses below $\approx 8 M_{\odot}$, can be used to deduce the geology of exoplanetary systems (e.g., Zuckerman et al. 2007; Farihi et al. 2013; Harrison et al. 2018; Putirka & Xu 2021). This is possible because many white dwarfs accrete material from reservoirs within their own planetary system (Jura 2003; Koester et al. 2014). Once this material reaches the photosphere of the white dwarf, its constituent metals, here defined as elements heavier than He, can be detected from their absorption lines in the observed spectrum.

By using atmospheric models to predict synthetic spectra, the relative abundances of these metals can be measured. Given this composition and further corrections for differential atomic diffusion where the overall composition of the accreted material can be estimated (e.g., Fontaine et al. 2015a,b; Koester et al. 2020), we may utilise geological modelling (e.g., Buchan et al. 2022), or comparison against known Solar System bodies (e.g., Swan et al. 2023), to infer its geological history. In order to draw any geological inferences from relative metal abundances, a minimum of 2 metals must be detected.

As of September 2024, there are 1739 white dwarfs with reliably detected photospheric pollution (Williams et al. 2024). The majority of polluted white dwarfs only have 1 metal detected (typically Ca), leaving 376 which are potentially amenable to geological analysis (Williams et al. 2024). The number of such systems is set to increase by an order of magnitude in the coming years. Surveys including 4MOST, WEAVE-WD, DESI and SDSS will between them provide medium-resolution spectroscopy for upwards of 150 000 white dwarfs.

Geological analysis of material accreted by white dwarfs suffers from a major caveat: the material which we measure in the photosphere does not necessarily have the same composition as what was actually accreted. This is because all metals sink through the atmosphere or interior of the white dwarf, and different metals sink on different timescales (Paquette et al. 1986a,b; Dupuis et al. 1992; Koester 2009). All else being equal, elements which sink on shorter timescales will appear relatively depleted, a phenomenon called ‘differential sinking’. Any attempt to model geology based on white dwarf pollution must take differential sinking into account.

Calculating these timescales requires detailed modelling of the atmosphere and envelope of the white dwarf. This includes the follow-

* E-mail: andy.buchan@warwick.ac.uk (AMB)

ing four key transport processes and their uncertainties (see [Bédard 2024](#) for a recent review).

Atomic diffusion. This refers to the collective effect of microscopic diffusion processes (gravitational settling, thermal diffusion, chemical diffusion, and radiative levitation), which is a function of atomic mass and charge and is thus different for each element. In white dwarfs, the dominant contribution is provided by gravitational settling ([Paquette et al. 1986b](#)). Modelling this process requires two key pieces of input physics: the ionisation state and diffusion coefficient of each element. In most existing calculations, ionisation states are obtained from a simple Thomas–Fermi or Hummer–Mihalas equation of state, while diffusion coefficients are based on a collision integral formalism using a screened Coulomb interaction potential ([Paquette et al. 1986a; Stanton & Murillo 2016](#)). Recent improvements based on average-atom models and effective potential theory have shown that these traditional assumptions break down in cool He-dominated envelopes, leading to large systematics in diffusion timescales ([Heinonen et al. 2020](#)). However, these improved calculations were limited to only two elements (Si and Ca) due to computational costs, and therefore current complete grids of diffusion timescales still rely on the older framework ([Fontaine et al. 2015a; Bauer & Bildsten 2019; Koester et al. 2020](#)).

Convection. As white dwarfs cool, convection develops in their outer envelope due to the recombination of the main chemical constituent. The convection zone appears when the effective temperature, T_{eff} , drops below about 18 000 K in H-dominated white dwarfs ([Cunningham et al. 2019](#)), and about 50 000 K in He-dominated white dwarfs ([Cukanovaite et al. 2021](#)). Because convection generates efficient chemical mixing, differential sinking can only operate below the convective region, where the diffusion timescales are longer than at the surface. In most studies, the depth of the convection zone has been predicted using 1D envelope models and the mixing-length theory ([Böhm-Vitense 1958](#)). This procedure depends on many physical ingredients and assumptions, notably the H/He radiative opacity and equation of state, the atmospheric boundary condition, and the assumed mixing-length parameter ([Tassoul et al. 1990; Fontaine et al. 2001](#)). In the last decade, 3D hydrodynamical simulations have produced a new state-of-the-art treatment of white dwarf convection ([Tremblay et al. 2013; Kupka et al. 2018; Cukanovaite et al. 2019; Cunningham et al. 2019, 2021](#)). These simulations crucially remove the need for the mixing-length parameter to describe the convective efficiency, but still rely on the same input microphysics.

Convective overshoot. This refers to the process by which convective cells can enter into underlying, formally stable, layers of the white dwarf ([Freytag et al. 1996; Cunningham et al. 2019; Kupka et al. 2018](#)). Convective overshoot effectively extends the depth of the uniformly mixed region, and forces differential sinking to take place in deeper layers, also increasing the inferred rate of accretion. In 1D models, the extent of convective overshoot is essentially a free parameter, usually expressed as some fraction of the pressure scale height ([Koester et al. 2020; Bédard et al. 2022a](#)). In 3D models, this feature is instead predicted from first principles, thus providing a much greater constraining power. However, 3D overshoot studies have so far only been performed for warm ($11\,000 \text{ K} \lesssim T_{\text{eff}} \lesssim 18\,000 \text{ K}$) H-dominated white dwarfs ([Cunningham et al. 2019](#)).

Thermohaline mixing. This is an instability which may be triggered by the inverted composition gradient caused by the accretion of heavy elements onto the H/He envelope ([Deal et al. 2013; Wachlin et al. 2017; Cresswell et al. 2025](#)). If such an instability is active, it would lead to extremely rapid sedimentation of metals, dramatically increasing the inferred rate of accretion. A secondary effect, more relevant to this work, is that all metals would sink on similar

timescales, effectively rendering differential sinking inactive ([Bauer & Bildsten 2018](#)). This may, in turn, lead to a change in the interpretation of the composition of the accreted material. Thermohaline mixing is expected to be important in H-dominated white dwarfs, but not in their He-dominated counterparts ([Deal et al. 2013; Bauer & Bildsten 2019](#)).

Differing treatment of these processes can influence the inferred metal sinking timescales of polluted white dwarfs, and could therefore influence the inferred geological history of accreted material. In this work, we investigate the circumstances under which different assumptions and techniques can result in different relative metal sinking timescales, and how this affects the geological interpretation.

This paper is structured as follows. In Sections 2 and 3 we introduce physical concepts which are key for all the test cases we consider. In Section 4 we introduce the diffusion timescale grids and physical models used to describe the variables in each test case. In Sections 5 and 6, we address the uncertainties due to convective overshoot and thermohaline mixing, respectively. In Section 7, we estimate the overall effect of other physical assumptions by comparing available grids of sinking timescales. In each of Sections 5–7, we start by identifying white dwarfs which are most likely to be affected, then assess the impact of changing the underlying physics, and finally discuss the results and broader implications. Section 8 highlights systems for which there is no such impact, and so have robust geological interpretations. We summarise our work in Section 9.

2 DIFFERENTIATION AND INCOMPLETE CONDENSATION

In this work, the geological processes which we focus on are core–mantle differentiation and incomplete condensation. These are the two most important processes in setting the Earth’s bulk composition and first order structure ([McDonough 2003; Wang et al. 2019](#)).

Incomplete condensation refers to a process that depends on the local temperature of a nascent body, which in turn is set by its distance from its host star. If this temperature is sufficiently high, as in the case of Earth, volatile elements cannot (completely) condense into the body and the resulting composition is depleted in volatile metals, including O, Na, C and N (e.g., [Wang et al. 2019](#)). Bulk-Earth-like devolatilisation has been detected in white dwarf pollutants (e.g., [Xu et al. 2014; Harrison et al. 2021; O’Brien et al. 2025](#)). More extreme heating can cause more moderately volatile elements to become depleted, or equivalently for refractory elements such as Ca, Ti and Al to become enriched, resulting in compositions analogous to thermally processed meteorite populations in the Solar System (e.g., [Xu et al. 2013](#)).

Core–mantle differentiation refers to the process by which a body such as Earth segregates into an iron-rich core and a silicate mantle. This does not affect the bulk composition of the body. However, if the body is subsequently fragmented in some way (the details of which we are agnostic towards), those fragments may, in general, be enriched in core- or mantle-like material. Accretion of a core-rich fragment would result in pollution high in siderophile elements such as Fe and Ni (e.g., [Wilson et al. 2015](#)). Accretion of a mantle-rich fragment is detectable by enrichment in lithophile elements such as Mg and Ca, relative to the siderophile elements (e.g., [Zuckerman et al. 2011](#)).

3 PHASES OF ACCRETION

The correction which is required in order to account for differential sinking depends on the phase of accretion. We denote the duration of an accretion event as t_{event} , and assume that mass accretes, starting at time $t = 0$, at a constant rate during this event before abruptly stopping, as in [Koester \(2009\)](#). Denoting the average metal sinking timescale as $\bar{\tau}$, we can identify three distinct possible phases of accretion that result as t increases.

For $t \ll \bar{\tau}$, the photospheric metal abundances rapidly increase, and their relative abundances closely match the composition of the accreted material (assuming that the atmosphere was pristine prior to accretion). This is the ‘build-up’ or ‘increasing’ phase. For $\bar{\tau} \ll t < t_{\text{event}}$, it can be shown that the photospheric abundances of all metals plateau, and the relative abundance of a given metal (compared to the accreted material) is weighted by its sinking timescale. This is known as the ‘steady state’ phase. For $t > t_{\text{event}}$, it can be shown that a given photospheric metal abundance decreases exponentially, at a rate which depends on the sinking timescale of that metal. This is the ‘declining’ or ‘decreasing’ phase. In this phase, the abundance ratio of any pair of metals diverges exponentially towards 0 or infinity. We can anticipate that for systems in the declining phase of the accretion, the impact of any change in the adopted sinking timescales will be greatest. If $\bar{\tau} \gtrsim t_{\text{event}}$, the system does not reach steady state, but passes straight from build-up to declining phase. For further details, see [Koester \(2009\)](#).

In a more realistic treatment, the accretion rate may exponentially decay over time ([Jura et al. 2009](#)). In such a model, there is no steady state phase, although analogues of the build-up and declining phases still exist. This can affect the resulting geological interpretation ([O’Brien et al. 2025](#)). Consideration of this effect is beyond the scope of this work.

4 METHODS

Our strategy is to model the metal abundances at white dwarfs using a Bayesian framework, identifying evidence for differentiation and/or incomplete condensation. We model each system twice, using different sinking timescales (or a different treatment of thermohaline mixing), according to the specific test being conducted. We aim to identify white dwarfs for which the geological interpretation is affected.

This section describes our Bayesian framework, our timescale grids and our implementation of thermohaline mixing. We also define 5 tests which make use of these different physical treatments, and describe our selection of samples of white dwarfs where these different assumptions are most likely to affect the geological interpretation of their pollution.

4.1 Bayesian modelling

We use the Bayesian framework implemented in `PyllutedWD` ([Harrison et al. 2018; Buchan et al. 2022](#)). This framework fits a number of geological models to the metal abundances inferred for a particular white dwarf and identifies the best one (i.e., that with highest Bayesian evidence¹). The Bayesian framework can identify evidence

¹ The best model is not necessarily the one which can fit the data best. The Bayesian evidence is a trade-off between goodness-of-fit and simplicity, i.e., fewer model parameters, and correspondingly fewer geological processes.

for core–mantle differentiation and/or incomplete condensation and quantify the sigma significance of that evidence.

We have updated the framework such that the absolute abundance of photospheric metals is now set by the mass of the accreted body. The prior distribution corresponds to a collisional cascade, such as might be generated when rocky bodies encounter the Roche limit of a white dwarf ([Wyatt et al. 2014; Kenyon & Bromley 2017](#)). For an ideal collisional cascade, the number density of bodies in mass range m to $m + dm$ is proportional to $m^{-11/6}dm$ ([Dohnanyi 1969](#)). This distribution penalises high masses (and, by extension, high accretion rates). We set the upper and lower mass limits to 6.0×10^{24} kg (approximately the mass of Earth) and $10^{13.5}$ kg respectively. These limits are arbitrary, but cover a broad enough range for the purposes of this work. Outside of this modification, and the changes described in Sections 4.2 and 4.3, the framework is not significantly changed from the version described in [Buchan et al. \(2022\)](#).

4.2 Sinking timescale grids

We consider various grids of sinking timescales based on two white dwarf modelling codes: the Koester envelope code ([Koester et al. 2020](#)) and the STELUM evolution code in its static mode ([Bédard et al. 2022a](#)). In the latter case, the stellar structure is computed with STELUM itself, but the diffusion timescales are then computed with separate routines², originally based on the work of [Paquette et al. \(1986a,b\)](#) with updates described in [Fontaine et al. \(2015a\)](#) and [Heinonen et al. \(2020\)](#). We still refer to these grids as STELUM grids for conciseness. We briefly describe the similarities and differences between the Koester and STELUM frameworks which are relevant to this paper.

For the H/He envelope structure calculations, both codes rely on the equation of state of [Saumon et al. \(1995\)](#) and the OPAL radiative opacities of [Iglesias & Rogers \(1996\)](#). For the outer boundary condition, the Koester code uses non-grey atmospheres ([Koester 2010](#)); for He-rich models, where traces elements can dominate the overall opacity, the atmospheres optionally include a fixed H abundance and various metal abundances. The STELUM models used in this work adopt a more approximate treatment using grey atmospheres and, for He-rich models, OPAL envelope opacities with a fixed metallicity to roughly account for the effect of trace elements. Improvements to this aspect of the code are currently being made and will be reported in a future publication. Both the Koester and STELUM codes describe convection following the ML2 version of the mixing-length theory ([Tassoul et al. 1990](#)), but assume different mixing-length parameter values of 0.8 and 1.0, respectively. For the diffusion calculations, both frameworks rely on diffusion coefficients obtained from the screened Coulomb potential formalism ([Paquette et al. 1986a; Stanton & Murillo 2016](#)). However, they use different metal ionisation models, i.e. Thomas–Fermi for the Koester code ([Feynman et al. 1949](#)) and Hummer–Mihalas for the STELUM framework ([Hummer & Mihalas 1988](#)).

Of particular interest for this paper is the treatment of convective overshoot. In the Koester code, overshoot is included by simply increasing the size of the convectively mixed region by an arbitrary amount, expressed in terms of the pressure scale height. STELUM also has this option but generally adopts a more physically motivated description, based on the expectation that the velocity of the convective flows decreases exponentially with depth ([Freytag et al. 1996](#);

² The practical reason is that the current version of STELUM includes detailed equations of state only for H, He, C, and O.

Cunningham et al. 2019). The mixing coefficient D due to overshoot at radial depth r can then be parametrised as:

$$D(r) = D_0 \exp\left(\frac{-2|r - r_0|}{fH_0}\right), \quad (1)$$

where r_0 , H_0 , and D_0 are the radial depth, pressure scale height, and mixing coefficient at the base of the convection zone, respectively, and f is the free parameter controlling the extent of overshoot. The boundary of the overshoot region is then taken as the depth where the mixing coefficient becomes smaller than the atomic diffusion coefficient.

In this work, we use six grids of sinking timescales based on either the Koester or STELUM framework and various treatments of convective overshoot. These grids, and their abbreviated names used in the rest of the paper, are as follows.

- Koester, without overshoot (KN)
- Koester, with fixed overshoot of one pressure scale height (KF)
- STELUM, without overshoot (SN)
- STELUM, with fixed overshoot of one pressure scale height (SF)
- STELUM, with overshoot predicted from equation (1) with variable f following Bédard et al. (2023) (SV)
- STELUM, with overshoot directly calibrated from the 3D simulations of Cunningham et al. (2019) (S3D)

The KN and KF timescales are directly sourced from the tables presented in Koester et al. (2020) and publicly available online³. For He-dominated white dwarfs, we use the ‘DBAZ’ grids, which rely on metal-polluted atmosphere models and thus have the Ca abundance as an additional parameter ($-15 \leq \log \text{Ca/He} \leq -7$, with other elements scaled to Ca assuming bulk Earth composition). KN ignores overshoot, while KF includes overshoot down to a fixed depth of one pressure scale height. This specific depth reflects the most conservative prediction available from Cunningham et al. (2019) across the simulated T_{eff} range.

We calculated the STELUM SN and SF grids as counterparts to the Koester KN and KF grids. We also calculated two additional STELUM grids using more realistic treatments of overshoot. In the SV grid, we use equation (1) with the f parameter varying according to the depth of the formal convection zone, as suggested in Bédard et al. (2023). More specifically, let q_0 denote the fractional mass depth of the convection zone ($q \equiv 1 - m_r/M_*$, where m_r is the mass within radius r and M_* is the total mass). For H-rich models, we assume $f = 0.80$ if $\log q_0 \leq -16$, $f = 0.05$ if $\log q_0 \geq -10$, and a linear interpolation in between. For He-rich models, we assume $f = 0.80$ if $\log q_0 \leq -12$, $f = 0.05$ if $\log q_0 \geq -6$, and a linear interpolation in between. These parametrisations are such that the overshoot region is relatively large at high T_{eff} when the convection zone is shallow, and becomes smaller as T_{eff} decreases and the convection zone deepens (see Figure 1 of Bédard et al. 2023). Our assumptions are designed to roughly match both 3D simulations of shallow convection (Cunningham et al. 2019) and constraints on deep convection obtained from 1D modelling of C dredge-up in cool He-rich white dwarfs (Bédard et al. 2022b). Finally, in the S3D grid, the depth of the overshoot region is directly taken from the 3D predictions of Cunningham et al. (2019). This approach is the most reliable but is currently limited to warm ($11\,000 \text{ K} \lesssim T_{\text{eff}} \lesssim 18\,000 \text{ K}$) H-dominated white dwarfs, hence the need for the other grids. Key information about our six timescale grids, including the range of temperature and surface gravity covered, is summarised in Table 1.

³ <https://www1.astrophysik.uni-kiel.de/~koester/astrophysics/astrophysics.html>, accessed 2023 October 05

We note that the physical assumptions of the SN grid are very similar to those underlying the sinking timescales that have been publicly available so far on the Montreal White Dwarf Database (MWDD; Dufour et al. 2017)⁴. Because the latter are based on an older version of STELUM (Fontaine et al. 2015a,b), the two sets of timescales are not strictly identical, but relative timescales typically agree within a few percent. The largest differences are seen for He-dominated atmospheres due to the MWDD assuming a mixing-length parameter of 1.25 (rather than our value of 1), while for H-dominated atmospheres the differences are purely numerical and thus much smaller. Therefore, our comments on the SN grid in this work are also applicable to the MWDD timescales⁵.

4.2.1 Simultaneous use of the S3D and SV grids

The temperature range of the S3D grid is relatively narrow ($11\,000 \text{ K} \leq T_{\text{eff}} \leq 20\,000 \text{ K}$) compared to the other STELUM grids for H-dominated white dwarfs ($5\,000 \text{ K} \leq T_{\text{eff}} \leq 30\,000 \text{ K}$). For the purposes of exploring the parameter space fully, when using the S3D grid we fill out the full temperature range by using values from the SV grid when $5\,000 \text{ K} \leq T_{\text{eff}} \leq 11\,000 \text{ K}$ or $20\,000 \text{ K} \leq T_{\text{eff}} \leq 30\,000 \text{ K}$. This represents the current fullest possible treatment of overshoot for H-dominated systems.

Throughout the rest of this work, unless otherwise noted, the S3D grid should be taken to mean the extended version of the S3D grid which includes values from the SV grid.

4.3 Thermohaline mixing

We implement a simplified treatment of thermohaline mixing for H-dominated white dwarfs in our forward model following Bauer & Bildsten (2018, 2019). For a given accretion rate \dot{M} , effective temperature T_{eff} and surface gravity $\log(g)$, we interpolate on a grid of MESA model outputs⁶ which quantify the strength of thermohaline mixing in terms of a factor which we denote χ . This factor is defined by the equation

$$\chi = \log_{10}\left(\frac{S_{\text{Ca}}^+}{S_{\text{Ca}}^-}\right), \quad (2)$$

where S_{Ca} is the surface abundance of Ca and is calculated both with and without thermohaline mixing (labelled + and – respectively). Since thermohaline mixing causes more rapid transport of metals away from the surface, we generally have $S_{\text{Ca}}^+ < S_{\text{Ca}}^-$ and therefore $\chi < 0$. Because of this behaviour, χ can be thought of as a ‘dilution factor’ for the accreted mass present in the photosphere.

When thermohaline mixing is switched on in our code, we scale all metal abundances by a factor of χ . Additionally, if $\chi < \log_{10}(0.5)$, we consider that thermohaline mixing is strong enough to effectively disable differential sinking (Bauer & Bildsten 2018). In this case, the relative photospheric metal abundances are fixed to equal those of the pollutant. This differs from the default, non-thermohaline, treatment because it removes the weighting associated with individual metal sinking timescales.

If the system has reached the declining phase of accretion, such that

⁴ <https://www.montrealwhitedwarfdatabase.org/evolution.html>

⁵ This refers to the MWDD timescales prior to this work, as we plan to implement our new timescales on the MWDD in the near future; see data availability statement.

⁶ Available at https://github.com/evbauer/DA_Pollution_Tables

Table 1. Summary of the diffusion timescale grids used in this work. Atm refers to the dominant chemical element in the atmosphere of the white dwarf. The final row shows the approximate grid range for the thermohaline dilution factor χ described in Section 4.3. Here, the boundaries are approximate because the MESA models are not defined by $T_{\text{eff}}/\log(g)$.

Grid	Code	Atm	Min T_{eff} /[K]	Max T_{eff} /[K]	Min $\log(g)$	Max $\log(g)$	ML2/α convection	Overshoot parametrisation
SN	STELUM	H	5000	30 000	7.5	9.0	1.0	None
		He	7000	30 000	7.5	9.0	1.0	None
SF	STELUM	H	5000	30 000	7.5	9.0	1.0	Fixed
		He	7000	30 000	7.5	9.0	1.0	Fixed
SV	STELUM	H	5000	30 000	7.5	9.0	1.0	Variable
		He	7000	30 000	7.5	9.0	1.0	Variable
S3D	STELUM	H	11 000	20 000	7.5	9.0	1.0	3D
		He	-	-	-	-	-	-
KN	Koester	H	5000	20 000	7.5	8.5	0.8	None
		He	3000	15 000	7.5	8.5	0.8	None
KF	Koester	H	5000	20 000	7.5	8.5	0.8	Fixed
		He	3000	15 000	7.5	8.5	0.8	Fixed
Thermohaline dilution factor χ	MESA	H	≈6000	≈20 500	≈7.5	≈8.5	-	-

the time of observation t is greater than the time when accretion ends t_{event} , the above adjustments are made at time t_{event} . We then divide the metal abundances by a correction factor equal to $(t - t_{\text{event}}) / \tau_X$ for each element X where τ_X is its sinking timescale. This ensures that elements decay away in the declining phase as expected following the end of the accretion event, using the adjusted abundances as a starting point.

We implement additional logic to handle parameter values beyond the edges of the grid outlined in Table 1. Extremely high accretion rates and high temperatures are snapped to the nearest grid edge. For low accretion rates, we set $\chi = 0$ at $\dot{M} = 1 \text{ g s}^{-1}$ and linearly interpolate between this boundary condition and the lowest \dot{M} value in our grid. This forces thermohaline mixing to become inactive for sufficiently low \dot{M} , even for values of temperature and surface gravity which always have thermohaline mixing active within the grid boundaries. For very low temperatures, we return $\chi = 0$; i.e., we assume thermohaline mixing is never active when $T_{\text{eff}} \lesssim 6000 \text{ K}$. This boundary is set by the edge of the MESA grid, although we expect thermohaline mixing to be less relevant at low temperatures in any case since very high accretion rates are required to trigger it. We have no particular logic for extreme values of $\log(g)$, but the grid range is broad in this dimension (covering roughly 7.5 to 8.5 in cgs units) so we simply restrict our attention to white dwarfs falling into this range.

4.4 Test cases

We define five test cases which form the core of this work, numbered from Test 1 to Test 5, which are summarised in Table 2. Tests 1 and 2 investigate convective overshoot, Test 3 investigates thermohaline mixing, and Tests 4 and 5 relate to publicly available timescale grids.

The tests are primarily defined by a pair of timescale grids a and b , which specify the grids to be used in our Bayesian modelling. The exception is Test 3, which investigates the effect of switching on thermohaline mixing when using the full treatment of 3D convective overshoot in H-dominated atmospheres. In this test, we keep the timescale grid fixed (so there is no grid b), but alter whether or not thermohaline mixing is active.

4.5 Sample selection

We select a manageable sample of white dwarfs to model for each test scenario. We select all our samples from the Planetary Enriched White Dwarf Database (PEWDD⁷, Williams et al. 2024), using a number of criteria to identify appropriate white dwarfs which are most likely to be affected in each test case.

Firstly, we consider H- and He-dominated white dwarfs separately, so we filter by the appropriate atmospheric type. Secondly, we filter out any white dwarfs which fall outside the joint T_{eff} and $\log(g)$ range covered by both sinking timescale grids under consideration (i.e., we do not perform any timescale extrapolation). Thirdly, we impose a minimum number of ‘modellable elements’. This refers to the number of the following elements which were detected, and which have valid abundances and uncertainties: Al, Ti, Ca, Ni, Fe, Cr, Mg, Si, Na, O, C, N. These are the elements which can be modelled by `PyllutedWD`. Finally, for a given white dwarf, and a given pair of sinking timescale grids a and b , we calculate $M_{a,b}$, a metric measuring the likely impact of swapping a for b . For details, see the Appendix. We impose a minimum value of this metric. Table 2 includes the full set of criteria used to select each sample. The resulting samples may be found in Table 3.

For Test 1 only, the second grid (b) used in sample selection is the unmodified S3D grid, without the expanded temperature range (see Section 4.2.1). This is because, in this test, we wish to identify white dwarfs which can be modelled using the full 3D treatment of convective overshoot.

For Test 3, there is no grid b , so the selection criteria require some modification. This test concerns thermohaline mixing, the effect of which is to effectively disable differential sinking. We capture this effect by replacing b with a dummy grid in which sinking timescales are the same for all elements. We also impose the constraint that $10 000 \text{ K} \leq T_{\text{eff}} \leq 20 502 \text{ K}$. The upper limit is the highest temperature covered by the thermohaline mixing grid (although the shape of this grid is irregular). The lower limit approximates the temperature at which the impact of thermohaline mixing is expected to become small.

For Test 5, we increased the minimum required number of

⁷ <https://github.com/jamietwilliams/PEWDD>, commit 3b905e0, accessed 2024 December 12

Table 2. Summary of tests and white dwarf sample selection criteria. For Test 1, Grid b should be taken to mean the unexpanded version of the S3D grid (see Section 4.2.1).

Test number	Test type	Atmosphere	Grid a	Grid b	Min. elements	Min. metric
1	Overshoot	H	SN	S3D	2	1
2	Overshoot	He	SN	SV	2	1
3	Thermohaline	H	S3D	-	2	1
4	Public grids	H	SN	KN	2	1
5	Public grids	He	SN	KN	4	2

modellable elements and the minimum metric score in order to keep the sample size practical.

4.5.1 White dwarf atmospheric parameters

By default, we adopt the values of T_{eff} and $\log(g)$ as given in PEWDD from different literature sources, data and fitting techniques. However, in many cases, the values of these parameters are not based on state-of-the-art space-based photometry and astrometry (Gaia Collaboration et al. 2023), and several entries assume $\log(g) = 8.0$. Therefore, we quote an additional set of parameters in Table 3, using the ‘mixed’ atmosphere model values from Gentile Fusillo et al. (2021) for He-dominated white dwarfs, and ‘pure-H’ values for H-dominated white dwarfs. If the T_{eff} values differ by more than 2%, or the $\log(g)$ values differ by more than 0.04 dex, adopted as characteristic uncertainties of current white dwarf model atmospheres and photometric flux calibration (Elms et al. 2024), we run our model using both sets of parameter values, and comment on any impact where relevant. Atmospheric metal abundance estimates depend on the values of T_{eff} and $\log(g)$, so in general the *Gaia* atmospheric parameters will not be fully consistent with the metal abundances.

4.5.2 Corrections and assumptions for specific white dwarfs

GD133 has no formal error on Mg, but Xu et al. (2014) adopt a value of 0.2 dex in their analysis, so we do likewise. Klein et al. (2011) give no error on the Ni abundance for HS2253+8023, so we assume a nominal value of 0.2 dex. At the time of writing, PEWDD contains a typographical error inherited from Steele et al. (2021), in which an upper bound on the Ni abundance of WD 1124–293 is listed as an abundance with no error - we correct for this issue here.

5 CONVECTIVE OVERSHOOT

This section describes the results of Tests 1 and 2. These tests use only timescales calculated with STELUM, but with different treatments of convective overshoot. We consider H- and He-dominated white dwarfs separately.

5.1 H-dominated white dwarfs (Test 1)

Test 1 investigates the effect of including a full 3D treatment of convective overshoot, compared to no convective overshoot at all. We select a sample of white dwarfs to model with and without overshoot following the criteria outlined in Section 4.5. There are 112 entries in PEWDD for H-dominated white dwarfs with at least 2 modellable elements (defined in Section 4.5). Our selection criteria narrow this down to a sample of 7 entries, corresponding to 5 individual white dwarfs (note that white dwarfs may have multiple entries in PEWDD due to analysis with different data and/or methodology). These 7

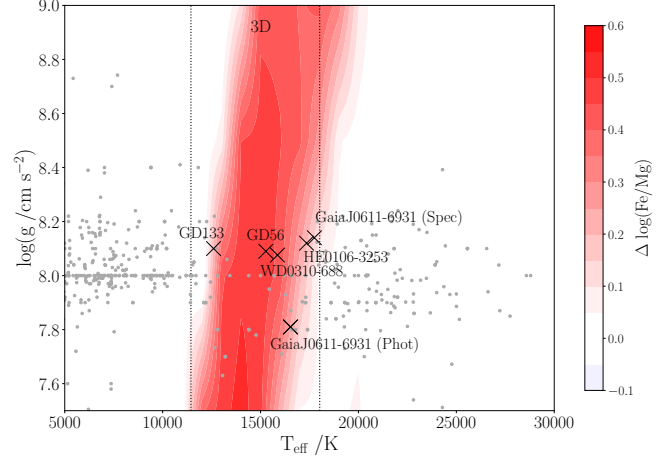


Figure 1. The change in relative sinking timescales for H-dominated white dwarfs when including 3D convective overshoot, compared to no overshoot, as a function of effective temperature (x axis) and surface gravity (y axis). The colour scale shows the change in the Fe/Mg sinking timescale ratio, on a log scale (base 10). Under the assumption of steady state accretion, the change in this ratio equals the change in the inferred Fe/Mg abundance ratio in the pollutant. The ratio is therefore significant when its absolute value is greater than the approximate uncertainty of metal abundances, typically 0.1 to 0.2 dex. The crosses indicate our sample of H-dominated white dwarfs which were modelled individually with these different treatments of overshoot (Test 1). The grey dots show all other H-dominated white dwarfs in PEWDD. Points may overlap when an individual white dwarf has multiple entries in PEWDD. For example, the GaiaJ0611–6931 (Phot) point corresponds to two entries (both listed explicitly in Table 3). The vertical dashed lines indicate the temperature range where convective overshoot has been explored with 3D simulations (as in the S3D grid). Outside of this range, we use the SV grid.

Table 3. Summary of the 5 samples of white dwarfs selected from PEWDD using the criteria outlined in Table 2. ME is the number of modellable elements. MS is the metric score. Sources: (1) [Rogers et al. \(2024a\)](#), (2) [Xu et al. \(2014\)](#), (3) [Xu et al. \(2019\)](#), (4) [Limbach et al. \(2024\)](#), (5) [Klein et al. \(2011\)](#), (6) [Hollands et al. \(2021\)](#), (7) [Hoskin et al. \(2020\)](#), (8) [Farihi et al. \(2011\)](#), (9) [Izquierdo et al. \(2020\)](#), (10) [Blouin et al. \(2018\)](#), (11) [Melis & Dufour \(2017\)](#), (12) [Gänsicke et al. \(2012\)](#), (13) [Kawka & Vennes \(2012\)](#), (14) [Zuckerman et al. \(2011\)](#), (15) [O'Brien et al. \(2023\)](#), (16) [Kawka et al. \(2019\)](#), (17) [Steele et al. \(2021\)](#), (18) [Swan et al. \(2019\)](#), (19) [Vennes & Kawka \(2013\)](#), (20) [Tremblay et al. \(2020\)](#), (21) [Klein et al. \(2021\)](#), (22) [Gentile Fusillo et al. \(2017\)](#), (23) [Raddi et al. \(2015\)](#), (24) [Swan et al. \(2023\)](#), (25) [Xu et al. \(2017\)](#), (26) [Koester & Wolff \(2000\)](#), (27) [Badenas-Agusti et al. \(2024\)](#), (28) [Doyle et al. \(2023\)](#).

Name	PEWDD ID	PEWDD Identifier	Atm	PEWDD Teff /[K]	PEWDD Teff err /[K]	PEWDD log(g)	PEWDD log(g) err	Gaia Teff /[K]	Gaia Teff err /[K]	Gaia log(g)	Gaia log(g) err	ME	MS	Source
Test 1 (7 entries, 5 unique white dwarfs)														
Gaia J0611-6931	263	Gaia J0611-6931 (Phot; Opt) Rogers 2023	H	16 530	561	7.81	0.03	16 147	550	7.86	0.05	4	1.5	(1)
Gaia J0611-6931	264	Gaia J0611-6931 (Phot; UV) Rogers 2023	H	16 530	561	7.81	0.03	16 147	550	7.86	0.05	6	1.0	(1)
GD133	1037	GD133 Xu 2014	H	12 600	200	8.10	0.10	12 157	153	8.03	0.02	4	1.3	(2)
Gaia J0611-6931	1216	Gaia J0611-6931 (Spec; Opt) Rogers 2023	H	17 749	248	8.14	0.04	16 147	550	7.86	0.05	4	1.1	(1)
GD 56	1792	GD 56 Xu 2019	H	15 270	300	8.09	0.10	14 904	303	8.00	0.03	4	1.8	(3)
HE 0106-3253	1793	HE 0106-3253 Xu 2019	H	17 350	200	8.12	0.10	16 053	313	8.02	0.03	4	1.9	(3)
WD 0310-688	3543	WD 0310-688 Limbach 2024	H	15 865	263	8.08	0.02	15 865	263	8.08	0.02	3	1.8	(4)
Test 2 (12 entries, 9 unique white dwarfs)														
PG1225-079	160	PG1225-079 Model 1 Klein 2011	He	10 500		7.70		11 248	141	8.13	0.02	6	1.1	(5)
Gaia J0644-0352	583	Gaia J0644-0352 (Phot; Opt) Rogers 2023	He	17 000	327	7.98	0.02	17 587	761	8.01	0.07	8	1.3	(1)
SDSS J0956+5912	649	SDSS J0956+5912 (No Overshoot) Hollands 2022	He	8 100	100	8.02	0.04	9 053	458	8.06	0.14	8	1.5	(6)
SDSS J0956+5912	650	SDSS J0956+5912 (Overshoot) Hollands 2022	He	8 100	100	8.02	0.04	9 053	458	8.06	0.14	8	1.5	(6)
WD J2047-1259	809	WD J2047-1259 Hoskin 2020	He	17 970	170	8.04	0.05	17 802	660	8.12	0.06	7	2.0	(7)
GD 61	1274	GD 61 Farihi 2011	He	17 820		8.20		16 726	418	8.10	0.04	5	1.0	(8)
GD 424	1389	GD 424 (WHT) Izquierdo 2021	He	16 560	75	8.25	0.02	16 326	525	8.21	0.05	4	2.8	(9)
GD 424	1390	GD 424 (Keck) Izquierdo 2021	He	16 560	75	8.25	0.02	16 326	525	8.21	0.05	9	1.3	(9)
HS2253+8023	1461	HS2253+8023 Model 2 Klein 2011	He	14 400		8.40		13 587	238	8.16	0.03	8	1.5	(5)
HS2253+8023	1543	HS2253+8023 Model 3 Klein 2011	He	14 800		8.70		13 587	238	8.16	0.03	7	2.7	(5)
Ross 640	1832	Ross 640 Blouin 2018	He	8 070	140	7.92	0.01	8 964	78	8.08	0.02	4	1.0	(10)
WD 1232+563	3519	WD 1232+563 Xu 2019	He	11 787	423	8.30	0.06	12 110	725	8.05	0.13	7	1.8	(3)
Test 3 (13 entries, 8 unique white dwarfs)														
Gaia J0611-6931	263	Gaia J0611-6931 (Phot; Opt) Rogers 2023	H	16 530	561	7.81	0.03	16 147	550	7.86	0.05	4	1.2	(1)
Gaia J0611-6931	264	Gaia J0611-6931 (Phot; UV) Rogers 2023	H	16 530	561	7.81	0.03	16 147	550	7.86	0.05	6	2.5	(1)
SDSS J1043+0855	877	SDSS J1043+0855 Melis & Dufour 2017	H	18 330		8.05		16 067	997	7.96	0.10	8	1.0	(11)
GD133	1037	GD133 Xu 2014	H	12 600	200	8.10	0.10	12 157	153	8.03	0.02	4	1.4	(2)
Gaia J0510+2315	1214	Gaia J0510+2315 (Phot Opt) Rogers 2023	H	20 130	145	8.13	0.02	21 255	457	8.18	0.03	4	2.0	(1)
Gaia J0510+2315	1215	Gaia J0510+2315 (Phot UV) Rogers 2023	H	20 130	145	8.13	0.02	21 255	457	8.18	0.03	3	1.5	(1)
Gaia J0611-6931	1216	Gaia J0611-6931 (Spec; Opt) Rogers 2023	H	17 749	248	8.14	0.04	16 147	550	7.86	0.05	4	1.1	(1)
Gaia J0611-6931	1217	Gaia J0611-6931 (Spec; UV) Rogers 2023	H	17 749	248	8.14	0.04	16 147	550	7.86	0.05	6	2.6	(1)
G29-38	1468	G29-38 Xu 2014	H	11 820	100	8.40	0.10	11 528	206	8.04	0.03	8	1.6	(2)
PG 1015+161	1676	PG 1015+161 Gänsicke 2012	H	19 200	180	8.22	0.06	18 377	473	7.97	0.04	5	1.1	(12)
GD 56	1792	GD 56 Xu 2019	H	15 270	300	8.09	0.10	14 904	303	8.00	0.03	4	1.1	(3)
HE 0106-3253	1793	HE 0106-3253 Xu 2019	H	17 350	200	8.12	0.10	16 053	313	8.02	0.03	4	3.6	(3)
PG 1015+161	1794	PG 1015+161 Xu 2019	H	20 420	350	8.11	0.10	18 377	473	7.97	0.04	4	1.3	(3)

Name	PEWDD ID	PEWDD Identifier	Atm	PEWDD Teff /[K]	PEWDD Teff err /[K]	PEWDD log(g)	PEWDD log(g) err	Gaia Teff /[K]	Gaia Teff err /[K]	Gaia log(g)	Gaia log(g) err	ME	MS	Source
Test 4 (17 entries, 15 unique white dwarfs)														
NLTT 1675	22	NLTT 1675 Kawka 2012	H	6 020	50	8.04	0.07	6 022	91	8.05	0.05	4	1.3	(13)
NLTT 43806	27	NLTT 43806 Zuckerman 2011	H	5 900		8.00		5 808	51	8.17	0.03	9	2.3	(14)
WD J1935–3252	30	WD J1935–3252 O'Brien 2023	H	5 430	10	8.00	0.01	5 305	47	7.97	0.04	4	6.8	(15)
NLTT 7547	34	NLTT 7547 Spectral Kawka 2019	H	5 198	54	7.89	0.04	5 311	100	7.97	0.07	5	2.7	(16)
NLTT 7547	35	NLTT 7547 (Balmer) Kawka 2019	H	5 460	80	8.04	0.18	5 311	100	7.97	0.07	5	1.4	(16)
NLTT 7547	36	NLTT 7547 Balmer Kawka 2019	H	5 460	80	8.04	0.18	5 311	100	7.97	0.07	5	1.4	(16)
WD 1124–293	522	WD 1124–293 Steele 2021	H	9 367		7.99		9 401	82	7.99	0.02	3	1.1	(17)
WD2115–560	546	WD2115–560 Swan 2019	H	9 600	340	7.97	0.08	9 528	76	7.96	0.02	5	1.1	(18)
NLTT 25792	810	NLTT 25792 Vennes & Kawka 2013	H	7 903	16	8.04	0.03	7 837	112	8.10	0.04	4	1.8	(19)
WD2157–574	889	WD2157–574 Swan 2019	H	7 010	250	8.06	0.08	7 114	55	8.10	0.02	6	1.6	(18)
GD133	1037	GD133 Xu 2014	H	12 600	200	8.10	0.10	12 157	153	8.03	0.02	4	1.0	(2)
WD0354+463	1618	WD0354+463 Vennes & Kawka 2013	H	8 240	120	7.96	0.10					4	2.6	(19)
WDJ113444.64+610826.68	1783	WDJ113444.64+610826.68 Tremblay 2020	H	7 590	40	7.96	0.02	7 502	59	7.97	0.02	2	1.6	(20)
WD1455+298	1784	WD1455+298 Vennes & Kawka 2013	H	7 383	19	7.97	0.03	7 342	53	7.97	0.02	3	2.1	(19)
G74-7	1785	G74-7 Vennes & Kawka 2013	H	7 306	22	8.06	0.02	7 196	48	7.93	0.02	4	3.1	(19)
WD1257+278	1786	WD1257+278 Vennes & Kawka 2013	H	8 609	20	8.24	0.02	8 586	71	8.04	0.02	4	1.5	(19)
G 166-58	1790	G 166-58 Xu 2019	H	7 390	200	7.99	0.10	7 342	53	7.97	0.02	4	2.6	(3)
Test 5 (25 entries, 19 unique white dwarfs)														
PG1225–079	160	PG1225–079 Model 1 Klein 2011	He	10 500		7.70		11 248	141	8.13	0.02	6	2.8	(5)
GALEXJ2339	367	GALEXJ2339 Klein 2021	He	13 735	500	7.93	0.09	14 796	366	8.08	0.05	7	7.3	(21)
GD 17	540	GD 17 Gentile Fusillo 2017	He	8 300	500	8.00		9 150	158	8.11	0.04	5	5.3	(22)
PG1225–079	582	PG1225–079 Model 2 Klein 2011	He	10 800		8.00		11 248	141	8.13	0.02	6	2.7	(5)
GD 16	594	GD 16 Gentile Fusillo 2017	He	11 000	500	8.00		11 207	166	8.12	0.03	4	3.0	(22)
SDSS J0956+5912	649	SDSS J0956+5912 (No Overshoot) Hollands 2022	He	8 100	100	8.02	0.04	9 053	458	8.06	0.14	8	9.1	(6)
SDSS J0956+5912	650	SDSS J0956+5912 (Overshoot) Hollands 2022	He	8 100	100	8.02	0.04	9 053	458	8.06	0.14	8	9.1	(6)
SDSS J124231.07+522626.6	652	SDSS J124231.07+522626.6 Raddi 2015	He	13 000	300	8.00		12 571	611	8.08	0.11	8	3.3	(23)
WD1350–162	724	WD1350–162 Swan 2019	He	11 640	290	8.02	0.05	11 892	560	7.99	0.11	8	2.5	(18)
SDSS J1038–0036	781	SDSS J1038–0036 Hollands 2022	He	7 560	150	8.06	0.04	8 088	180	8.05	0.06	7	3.4	(6)
WD2216–657	785	WD2216–657 Swan 2019	He	9 190	210	8.05	0.05	9 821	101	8.07	0.02	4	4.2	(18)
J0939	854	J0939 Swan 2023	He	9 020	200	8.07	0.05	9 649	153	8.09	0.04	6	2.2	(24)
J1227	855	J1227 Swan 2023	He	7 420	80	8.07	0.04	7 947	295	8.07	0.11	6	2.4	(24)
HS2253+8023	989	HS2253+8023 Model 1 Klein 2011	He	14 000		8.10		13 587	238	8.16	0.03	8	2.5	(5)
J0956	1061	J0956 Swan 2023	He	8 720	100	8.13	0.05	9 053	458	8.06	0.14	9	3.6	(24)
PG1225–079	1404	PG1225–079 Model 3 Klein 2011	He	11 100		8.30		11 248	141	8.13	0.02	6	3.2	(5)
HS2253+8023	1461	HS2253+8023 Model 2 Klein 2011	He	14 400		8.40		13 587	238	8.16	0.03	8	2.6	(5)
WD 1425+540	1591	WD 1425+540 (Model 1) Xu 2017	He	14 490		7.95		14 549	233	8.07	0.03	8	3.1	(25)
WD 1425+540	1592	WD 1425+540 (Model 2) Xu 2017	He	14 490		7.95		14 549	233	8.07	0.03	8	3.6	(25)
L 745–46A	1606	L 745–46A Koester & Wolff 2000	He	7 500	200	8.00	0.20	7 650	53	7.98	0.02	4	3.5	(26)
WD 1232+563	1828	WD 1232+563 Badenas-Agusti 2024	He	11 778	86	8.24	0.06	12 110	725	8.05	0.13	6	2.6	(27)
Ross 640	1832	Ross 640 Blouin 2018	He	8 070	140	7.92	0.01	8 964	78	8.08	0.02	4	7.9	(10)
Gaia J0218+3625	2315	Gaia J0218+3625 Doyle 2023	He	14 700	500	7.86	0.05	15 848	652	7.94	0.08	9	2.1	(28)
WDJ183352.68+321757.25	3508	WDJ183352.68+321757.25 Tremblay 2020	He	7 650	60	8.05	0.02	7 743	156	7.93	0.05	5	11.3	(20)
WD 1232+563	3519	WD 1232+563 Xu 2019	He	11 787	423	8.30	0.06	12 110	725	8.05	0.13	7	3.9	(3)

entries, by construction, should be the most likely to be affected by the change in (relative) metal sinking times associated with switching on convective overshoot. However, it is not guaranteed that the geological interpretation will actually be affected: these are simply the strongest candidates according to our metric.

By construction, the sample falls within a fairly well-defined temperature range between about 12 000 K and 18 000 K, which is the range covered by 3D simulations (Cunningham et al. 2019). Within this range, we predict a significant discrepancy in relative sinking timescales, as shown in Figure 1. This figure only shows the change in the Fe/Mg sinking timescale ratio, but all ratios show qualitatively similar behaviour (see Appendix).

Of the 7 entries in our sample, 2 are qualitatively affected by the inclusion of overshoot: GD 56 and WD 0310–688. However, the statistical significance of the effect is low in both cases.

GD 56 serves as a useful case study. We use abundance data from Xu et al. (2019), who did not find evidence of any particular geological process for this white dwarf. Our results support this non-detection, but show that it could have been affected by overshoot. We find that, without overshoot, GD 56 is best explained as a core-rich fragment ($41_{-13}^{+14}\%$ by moles⁸) of material from a body which experienced incomplete condensation at $T = 358_{-209}^{+474}$ K. In contrast, when overshoot is taken into account, the best model is primitive material: there is no evidence for incomplete condensation, or for selective accretion of core-rich material. The difference between these 2 solutions is shown in Figure 2. The red and blue dashed lines show the (median) inferred composition of the accreted material with and without overshoot respectively. With no overshoot, a noticeable enrichment in siderophile elements (those found in the core, such as Fe, Ni and Cr) is inferred, relative to solar abundances. The enrichment is absent when including overshoot. This can be understood as a consequence of Fe sinking more slowly (relative to Mg) in this case (see Figure 1), such that a high initial abundance of Fe is no longer needed in order to explain its observed abundance.

The statistical significance of differentiation and incomplete condensation, when excluding overshoot, is relatively low (1.4σ in both cases). In other words, without including a complete treatment of overshoot, one might be led to conclude that there is evidence of core-mantle differentiation and incomplete condensation, but such evidence could be identified as tentative.

WD 0310–688 is also a useful case study. This system exhibits an infrared excess, possibly due to an orbiting exoplanet, and is also polluted by metals (Limbach et al. 2024). The metal pollution is consistent with accretion of bulk-Earth-like material. Similar to GD 56, our results support this conclusion, and show that it is dependent on convective overshoot, albeit weakly. The key element is ratio is O/Mg which is slightly depleted (relative to solar abundances). Without overshoot, this depletion can be explained as the effect of differential sinking: we have $\tau_O/\tau_{Mg} = 0.5$, such that O sinks out of the photosphere faster than Mg. However, when including overshoot, $\tau_O/\tau_{Mg} = 1.6$, and the best model now invokes oxygen depletion in the accreted material. The framework finds evidence (to 1.5σ significance) of incomplete condensation of volatiles in this case, comparable to bulk-Earth-like material rather than primitive material. Figure 3 illustrates the difference between the accreted material in the two cases, showing an inferred depletion of oxygen in the overshoot case.

Including convective overshoot causes the sinking timescales of O

⁸ Here, core-rich should be understood as relative to the parent body, whose molar core fraction is estimated to be 12%.

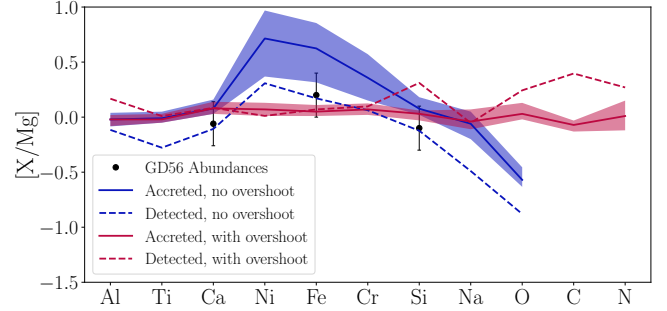


Figure 2. The geological interpretation of the metals accreted by GD 56 changes when convective overshoot is taken into account. The black data points, with 1 sigma error bars, show the abundances of metals in the photosphere of GD 56 on a log scale relative to Mg, and scaled to solar. The solid blue line shows the inferred composition of the accreted material when modelling the data without convective overshoot. The shaded blue region is a 1 sigma confidence interval. Our Bayesian framework finds (weak) evidence for core-mantle differentiation, with the best model invoking a core-rich composition. This composition should not be directly compared to the data points, because differential sinking causes the accreted and detected compositions to differ. The dashed blue line accounts for this correction, and may be compared with the data. For visual clarity, the 1 sigma confidence interval is omitted in this case. The red lines show the equivalent results when including convective overshoot using results from detailed 3D simulations. When taking this effect into account, the best model does not find any evidence of core-mantle differentiation. The compositions without overshoot (blue lines) predict negligible quantities of C and N, so these are not shown.

and Fe to increase by a greater factor than for the lithophile elements Ca and Mg (see Appendix). The inferred abundances of O and Fe in the accreted material therefore decrease. This results in a bias towards identification of mantle-rich and/or volatile-poor material. Similarly, identification of core-rich or volatile-rich material is hindered⁹. We have identified 2 systems for which this effect is relevant. In these cases, the effect is of low statistical significance, but does nevertheless change the geological interpretation.

5.2 He-dominated white dwarfs (Test 2)

There are 316 entries in PEWDD with a He-dominated atmosphere and at least 2 modellable elements, which our selection criteria narrow down to a sample of 12 (covering 9 unique white dwarfs). For most entries in our sample (9/12), there was no change (or only extremely marginal change) when including our best prescription of convective overshoot. However, this count includes two entries, HS 2253+8023 Model 2 and 3, which the Bayesian framework was unable to fit regardless of the treatment of overshoot. This is due to the high Ca abundance in these cases, particularly as compared to Ti and Si, relative to the small errors quoted for these metals. Our count also includes 2 entries for SDSS J0956+5912 from Hollands et al. (2021) which are identical for our purposes. The difference between these entries is whether convective overshoot was included in their metal accretion rate estimates, but those estimates are not used in this work, since we effectively recalculate them ourselves. Hollands et al. (2021) found no significant effect on the inferred composition of accreted material.

⁹ The sinking timescales of Si, which typically behaves as a lithophile, are increased by a factor slightly greater than that of Fe. But this effect is small, and Si can also exhibit siderophilic behaviour (Buchan et al. 2022).

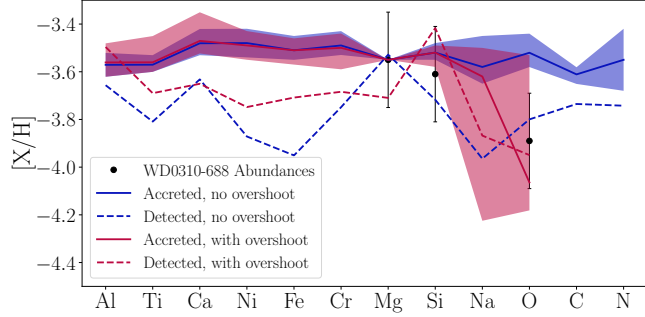


Figure 3. The geological interpretation of the metals accreted by WD 0310–688 changes when convective overshoot is taken into account (red). The interpretation of the plot features is similar to Figure 2, but the abundances are scaled to the dominant photospheric element, in this case H, rather than Mg. We choose this scaling in cases where one or more of the fits does not replicate the Mg abundance particularly well, such that scaling to Mg results in a non-representative illustration of the overall quality of that fit. For the accreted compositions, the vertical position is arbitrary, so we fix the Mg abundance to match the detected abundance (and therefore there is no uncertainty on the Mg abundance for the accreted compositions). Our Bayesian framework finds (weak) evidence for incomplete condensation only when including convective overshoot.

The 3 systems for which we nominally find an effect are Ross 640, WD 1232+563 and GD 424 (when using Keck data). For WD 1232+563 (Xu et al. 2019), our forward model strongly favours a particular value of the initial nebular composition, and so our results are specific to that value and do not sample a range as would normally be the case. While this is not necessarily unphysical, we conservatively exclude this system from the following discussion. The other two systems also come with caveats associated with the values of T_{eff} and $\log(g)$.

Ross 640 (Blouin et al. 2018) is similar to GD 56: differentiation is invoked only when ignoring convective overshoot (to 1.4σ). This is because Fe sinks faster (relative to other metals) when including overshoot, such that the Fe depletion can be explained as the consequence of differential sinking rather than accretion of mantle-like material (with molar core fraction $4 \pm 2\%$). But this discrepancy is only present when using the values of T_{eff} and $\log(g)$ found by Blouin et al. (2018) (as included in PEWDD). The equivalent values from Gentile Fusillo et al. (2021) using *Gaia* data are significantly higher (see Table 3), leading to different metal sinking timescales. When using these timescales, the discrepancy in interpretation is not present, leaving it ambiguous as to whether the treatment of convective overshoot is relevant for this system. However, the potential discrepancy is only minor in any case (1.4σ).

The results for GD 424, using data from the High Resolution Echelle Spectrometer (HIRES) at the Keck I telescope (Izquierdo et al. 2020), are illustrated in Figure 4. Differentiation is invoked only when including convective overshoot (to 2.6σ). Including overshoot does not strongly affect the sinking timescales of Ni or Fe relative to Mg in this case. With or without overshoot, the framework finds that accretion has reached the declining phase. However, with overshoot included, the best model finds that the system is not as deep into the declining phase of accretion, and that therefore the Ni and Fe depletion cannot be attributed to differential sinking. This result is driven by the Al abundance. With convective overshoot included, Al sinks on a (relatively) long timescale. If accretion had proceeded too deep into the declining phase, the predicted Al abundance, relative to other metals, would be too high. The best model

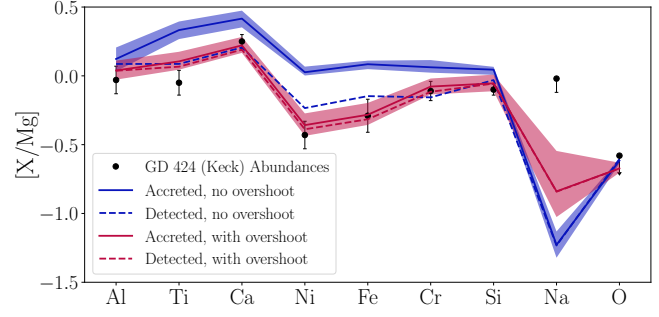


Figure 4. The geological interpretation of the metals accreted by GD 424 changes depending on whether convective overshoot is neglected (blue) or included (red). The plot features are similar to Figure 2.

now invokes accretion of a mantle-rich fragment (with molar core fraction $6 \pm 2\%$). Another entry for GD 424, corresponding to data from the Intermediate dispersion Spectrograph and Imaging System (ISIS) at the William Herschel Telescope (WHT), was found to show no change in interpretation when including overshoot. For this entry, there are no Ni, Fe or Cr abundances recorded, so it is not possible to infer the presence of differentiation. However, in all four cases (Keck and WHT data, with and without overshoot), the best model invokes incomplete condensation.

As with Ross 640, using the *Gaia* values for T_{eff} and $\log(g)$ removes any discrepancy in geological interpretation: with these parameters, differentiation and incomplete condensation are invoked regardless of whether overshoot is considered. The parameter values taken from Izquierdo et al. (2020) and Gentile Fusillo et al. (2021) are sufficiently close that they can be considered consistent within the systematic errors. This suggests that the geological modelling for this system is highly sensitive to the values of these parameters.

Izquierdo et al. (2020) favour a solution for this system in which the accreted material is similar to CI chondrites or bulk Earth, and accretion is ongoing. Core–mantle differentiation was not invoked. The declining phase was ruled out because it implies a high abundance of siderophile elements (although we note that this tension might potentially be eased by invoking differentiation followed by preferential accretion of mantle-like material). We also note that Izquierdo et al. (2020) used timescales based on Koester et al. (2020). One of the consequences is that, relative to timescales calculated using STELUM, high siderophile element abundances are more likely to be inferred. This will be discussed in Section 7.

5.3 Overview

So far, we have focussed on individual white dwarfs. We now consider the population of white dwarfs more broadly, and ask which regions of parameter space, as defined by T_{eff} and $\log(g)$, are most likely to host white dwarfs affected by the treatment of convective overshoot. To do this, we calculate the mean value of our discrepancy metric across parameter space. The metric is a function of β , the ‘depth’ of a system into its declining phase of accretion (see Appendix), and the abundances of the modellable elements.

We sample metal abundances from 50 000 synthetic polluted white dwarfs generated from Monte Carlo-style simulations similar to those described in Buchan et al. (2024). We do not describe this in detail, because the only practical output is a list of which elements are ‘detected’ for each white dwarf. White dwarfs with fewer than 2 detected elements are ignored.

For each synthetic white dwarf, we calculate the discrepancy met-

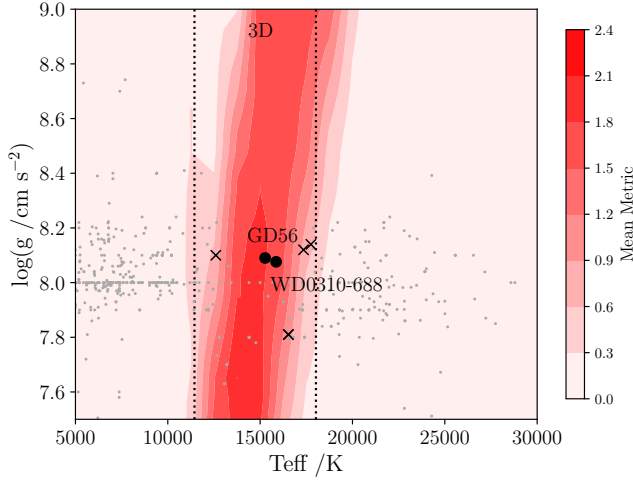


Figure 5. The susceptibility of H-dominated white dwarfs to a change in geological interpretation when including a full treatment of convective overshoot, compared to no overshoot, as a function of effective temperature and surface gravity. We show this in terms of the mean value of our discrepancy metric (see Section 5.3) for randomly generated synthetic white dwarfs. The metric does not take into account the specific abundances (and errors) of detected metals, which is important for predicting whether any particular polluted white dwarf will be susceptible. The metric is inversely proportional to the uncertainty on abundances - here we assume 0.2 dex errors. The sample used for Test 1 is shown with black crosses. The black circles show the subset of those systems for which the geological interpretation does actually change when using a full 3D parametrisation of convective overshoot. The grey dots show all other H-dominated white dwarfs in PEWDD.

ric 50 times, using different values for β . We sample β randomly from an exponentially decaying distribution with a decay parameter equal to the *a priori* probability of observation in the declining phase, p (see Equation 9). This parametrisation reproduces important, physically motivated, features. For white dwarfs with very short sinking timescales (e.g., warm and H-dominated), p is close to zero. Therefore, the sampled values of β are also close to zero and the declining phase contribution to the discrepancy metric is negligible, as expected. For white dwarfs with long sinking timescales (e.g., cool and He-dominated), p is close to 1, and the resulting distribution of β approximates the inferred distribution of β for cool DZs (see Figure 4.7 in Buchan 2023). Between these extremes, the distribution of β varies smoothly.

Figure 5 shows that this approach reproduces the sensitive regime between about 12 000 K and 18 000 K that was visible in Figure 1. This is expected, because in this case the sensitive regime is in roughly the same location for all possible pairs of detected metals that the discrepancy metric could sample (this is not the case generally). Almost any H-dominated white dwarf in the sensitive regime could be affected, depending on its exact metal abundances. This is roughly 12% of all H-dominated metal polluted white dwarfs (based on PEWDD).

Figure 6 shows the equivalent plot for He-dominated white dwarfs. The severely affected regions of parameter space are sparsely populated. This suggests that for most He-dominated white dwarfs, the impact of neglecting convective overshoot is likely to be minor. However, in some cases there may still be a significant impact, depending on the details of the white dwarf. In particular, white dwarfs with particularly small errors on their abundances are more likely to be impacted. Notably, all but one of the entries in our sample had at least 3 elements with particularly small errors (≤ 0.1 dex). It should

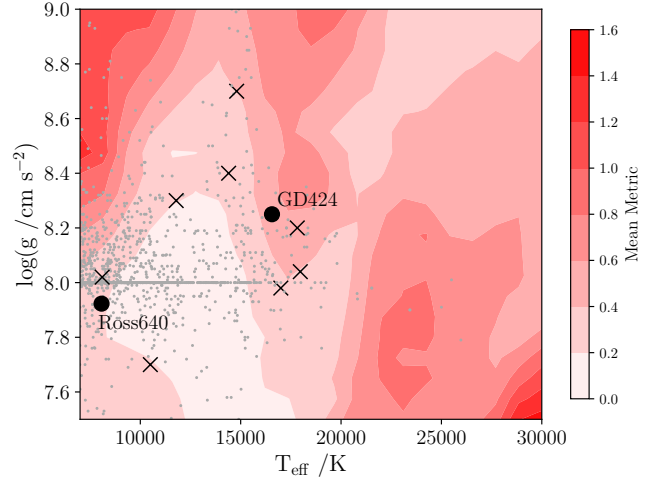


Figure 6. The susceptibility of He-dominated white dwarfs to a change in geological interpretation when including a detailed treatment of convective overshoot compared to no overshoot. The meaning of the colour bar and label types are similar to those in Figure 5, but the black markers show the sample for Test 2, and grey dots now correspond to He-dominated white dwarfs.

be noted that Figure 6 is based on a 1D parametrisation of overshoot, which has not been confirmed with full 3D simulations.

5.4 Treatment of convective overshoot

Broadly speaking, for H-dominated atmospheres, ignoring convective overshoot will cause inferred compositions to tend towards core- and volatile-rich, under the assumption that the accreted material formed through the same geological processes which are most significant in the formation of rocky Solar System bodies. We found that this effect is active within a temperature range of roughly 12 000 K to 18 000 K. For such white dwarfs, it is likely that accretion is in the steady state phase, limiting the potential discrepancy. Nevertheless, for such white dwarfs, convective overshoot should be considered in order to draw reliable geological conclusions. Below 11 000 K, we are reliant on a 1D model of convective overshoot. It is possible that convective overshoot may continue to be impactful below that temperature, but further 3D simulations probing this temperature range are required to draw firm conclusions.

For He-dominated white dwarfs, Figure 6 shows that the effect of convective overshoot itself is predicted to be relatively minor in most cases. The systems for which we nominally found some impact had unusually small errors on their metal abundances.

5.4.1 Fixed overshoot

So far, we have used what we consider to be the most complete, variable parametrisations of convective overshoot. In this section, we discuss a simpler treatment, in which the extent of overshoot is fixed to one pressure scale height. We investigate whether using fixed overshoot is preferable to using no overshoot, as benchmarked against a full treatment of overshoot (meaning either the S3D or SV grid for H- or He-dominated systems, respectively).

For H-dominated systems, outside of specific combinations of temperature and metals, the SO grid reproduces relative sinking timescales from the S3D grid better than the SN grid, implying that fixed overshoot is usually preferable to no overshoot. For He-dominated systems, the situation is more complicated. We illustrate

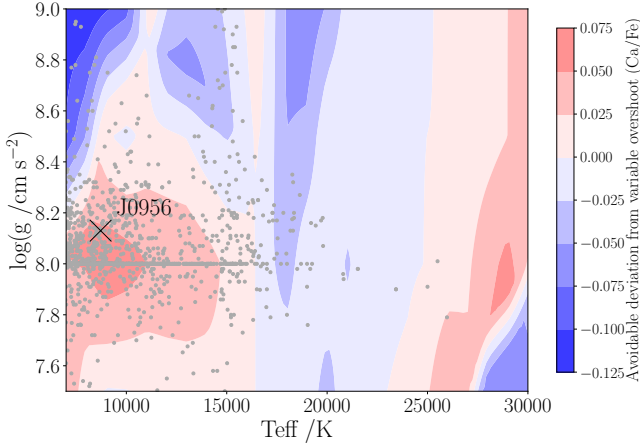


Figure 7. Plot showing which He-dominated white dwarfs (grey dots) are best modelled with no overshoot, or with fixed one pressure scale height overshoot, as benchmarked against a variable treatment of overshoot (SV grid) and using the Ca/Fe sinking timescale ratio. The red (positive) regions show parts of parameter space in which it is preferable to use no overshoot. In the blue (negative) regions, fixed overshoot is preferable. The magnitude shows the deviation (from the benchmark) that is avoided by using the preferred option (i.e., the greater the magnitude, the more strongly the relevant option should be preferred).

our results in Figure 7, looking at the timescale ratio of Ca/Fe (we find qualitatively similar behaviour for most combinations of Ca, Fe, O, Si and Mg). In Figure 7, the red (positive) regions show where it is preferable to use no overshoot. The blue (negative) regions are where fixed overshoot is preferable. The magnitude of the value indicates how strong the improvement is. Most He-dominated white dwarfs (grey dots) are best modelled using no overshoot, rather than fixed overshoot. Physically, this is because for white dwarfs of this approximate temperature, the extent of convective overshoot in the SV grid becomes small, such that no overshoot is a better approximation than one pressure scale height of overshoot.

As an example, we consider the white dwarf J0956, using data from [Swan et al. \(2023\)](#). When modelling the system with no overshoot (SN grid), or a full treatment (SV grid) of overshoot, core-mantle differentiation is invoked to 2.4σ significance. However, when including one pressure scale height of overshoot (SF grid), no evidence of differentiation is recovered (see Figure 8).

6 THERMOHALINE MIXING

This section covers the results of Test 3. This test differs from the others: rather than comparing the effect of switching between different grids of sinking timescales, we stick with one set of sinking timescales and test the impact of including thermohaline mixing on a sample of 13 entries from PEWDD with H-dominated atmospheres (corresponding to 8 white dwarfs). We select these entries using our metric, which estimates which white dwarfs are most likely to be affected by thermohaline mixing (Section 4.5). We illustrate the selected sample in Figure 9, which also shows the predicted strength of thermohaline mixing across $T_{\text{eff}}/\log(g)$ space. In Section 6.1, we discuss results for the white dwarfs highlighted in Figure 9. In Section 6.2, we discuss the effect of thermohaline mixing across the parameter space more generally. We also compare accretion rates, calculated with and without thermohaline mixing, against constraints from X-ray detections for G 29–38.

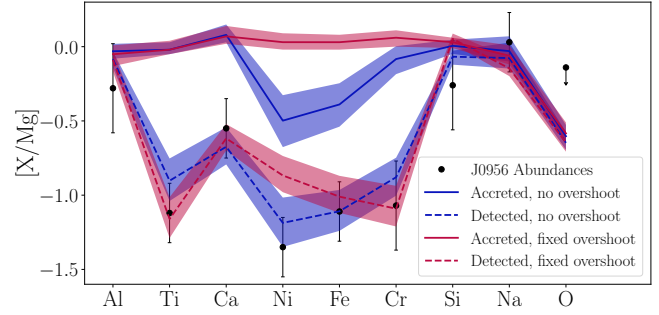


Figure 8. The geological interpretation of the metals accreted by J0956 changes when assuming no convective overshoot (blue) or overshoot fixed to one pressure scale height (red). The plot features are similar to Figure 2, but with the 1 sigma confidence intervals now also shown for the fits to the detected compositions. The Bayesian framework finds evidence for mantle-rich material, and therefore core-mantle differentiation, only when using no overshoot. The data point for O is an upper bound.

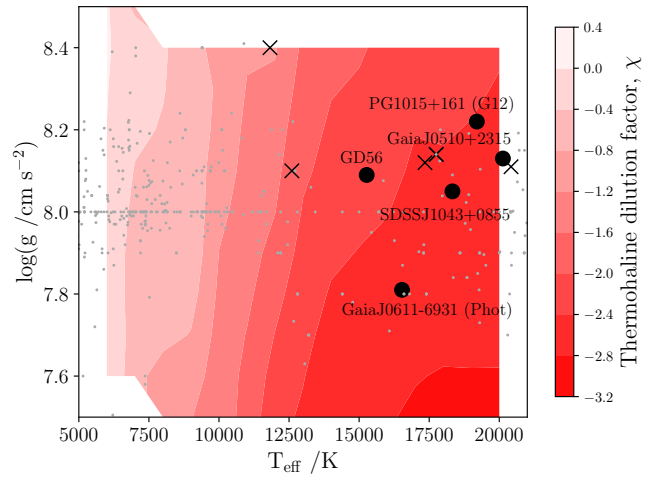


Figure 9. Strength of thermohaline mixing as a function of effective temperature and surface gravity for H-dominated white dwarfs. The strength is expressed as the dilution factor, χ , which quantifies the reduction of accreted mass remaining in the photosphere, due to thermohaline mixing (see Section 4.3). Here, we calculate χ assuming a fixed accretion rate of 10^9 g/s. The black markers show the white dwarfs included in our sample for Test 3, with circles indicating systems for which the geological interpretation changes when including thermohaline mixing. Grey dots show all H-dominated white dwarfs in PEWDD. Black crosses show the final sample which we model. The grid is irregular due to non-linear transformations between mass and surface gravity, and temperature and cooling age.

6.1 Results for individual systems (Test 3)

Two entries, SDSS J1043+0855 and PG 1015+161 (specifically the entry using data from [Gänsicke et al. 2012](#)), show changes in whether differentiation is invoked, depending on whether thermohaline mixing is considered. SDSS J1043+0855 is slightly depleted in Fe and Ni relative to Solar, but we find that this depletion can be explained solely as the result of differential sinking when thermohaline mixing is excluded. With thermohaline mixing included, differential sinking is ineffective, and the depletion is now inferred to be geological in nature (i.e., accretion of mantle-like material, to 2.4σ significance; see Figure 10). PG 1015+161 shows the opposite behaviour (for the same underlying reason), requiring core-like material (to 1.4σ sig-

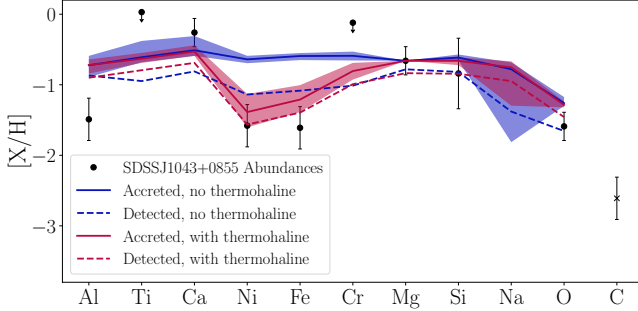


Figure 10. The geological interpretation of the metals accreted by SDSS J1043+0855 changes when including thermohaline mixing (red). The plot features are similar to Figure 3. The Bayesian framework finds evidence for accretion of mantle-rich material, and therefore core-mantle differentiation, only when including thermohaline mixing. The data points for Ti and Cr are upper bounds. The C data point was excluded during fitting because our incomplete condensation model does not accurately handle sub-Solar values of C. The C depletion implies incomplete condensation, which is inferred for all compositions shown here due to the O depletion.

nificance), but only when thermohaline mixing is not included. In this case, the fit to the data is poor (reduced $\chi^2 > 2$), but this is marginal and other models (with lower Bayesian evidence) are still able to fit the data well.

The results for both of these entries are sensitive to the values of T_{eff} and $\log(g)$. When adopting values from *Gaia* instead of spectroscopic parameters, we find that differentiation is invoked for SDSS J1043+0855, and is not invoked for PG 1015+161, regardless of whether thermohaline mixing is considered. We also note that Melis & Dufour (2017) concluded that SDSS J1043+0855 has accreted material from a differentiated body, using spectroscopic parameters and excluding thermohaline mixing, but using sinking timescales from an earlier version of STELUM.

The inferred volatile content is affected for 4/11 entries, with sigma significance varying between 1.3 and 2.0. For three of these (Gaia J0611–6931 (Phot; Opt), Gaia J0510+2315 (Phot Opt), Gaia J0510+2315 (Phot UV)), O is slightly depleted. Without thermohaline mixing this is explained via differential sinking, whereas with thermohaline mixing included the accreted material is inferred to be depleted in volatiles to some extent. These results depend on the values of T_{eff} and $\log(g)$. Rogers et al. (2024a) provide photometric and spectroscopic values, and Gentile Fusillo et al. (2021) provide additional values using *Gaia* data. Rogers et al. (2024a) also calculate metal abundances using both UV and optical data. We do not go through every combination here, but note that each of these choices can affect whether incomplete condensation is invoked. For GD 56, the sigma significance is low (less than 1.3), and the change in result can be attributed to random chance.

Both Gaia J0611–6931 and Gaia J0510+2315 have a detection (or upper bound) on C from UV data, indicating sub-Solar abundances (Rogers et al. 2024a). Our modelling does not include C if it is significantly sub-Solar, due to a known issue in the condensation code. If the C abundances were taken into account, it is likely that incomplete condensation would be invoked to some extent (see Rogers et al. 2024b). This could potentially resolve the ambiguity noted here.

6.2 Discussion

The region of parameter space in which thermohaline mixing is most relevant depends on multiple factors. The first factor is whether ther-

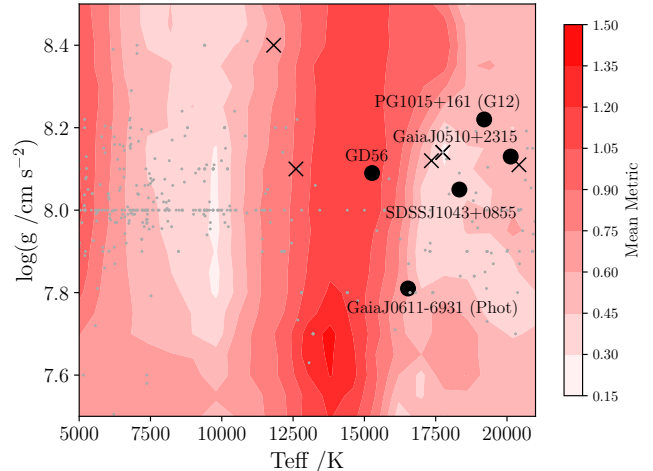


Figure 11. The susceptibility of H-dominated white dwarfs to disabling differential sinking, if thermohaline mixing is sufficiently strong. The crosses show the sample of white dwarfs used in Test 3. The black circles show the subset of those systems for which the geological interpretation changed when including thermohaline mixing. The grey dots show all other H-dominated white dwarfs in PEWDD. The metric here compares the S3D timescale grid against a dummy grid in which all sinking timescales are equal.

mohaline mixing is strong enough to deactivate differential sinking. Figure 9 shows the predicted strength of thermohaline mixing for H-dominated white dwarfs. The strength of thermohaline mixing is shown in terms of the change in mixed mass assuming a fixed accretion rate of 10^9 g s^{-1} . Broadly speaking, thermohaline mixing is stronger for hotter white dwarfs, leading to lower mixed masses for a given accretion rate. For our modelling purposes, the consequence is that, for a given mass of atmospheric metals, higher accretion rates are inferred. This does not, in and of itself, affect geological interpretation. However, in our prescription of thermohaline mixing, differential sinking is disabled if thermohaline mixing is sufficiently strong. This can affect geological interpretation if differential sinking would cause significant changes in the detected relative metal abundances. This is the second factor in determining the relevance of thermohaline mixing, and is illustrated in Figure 11. This figure shows the strength of differential sinking, using similar methodology to Figure 5, but comparing the timescales calculated using a full treatment of overshoot against a dummy grid of timescales. The dummy grid represents the case of no differential sinking, and contains the same value for every metal. Figure 11 shows that the white dwarfs which are most affected by the deactivation of differential sinking lie between approximately 12 000 K and 16 000 K. This temperature range is largely driven by the Si/Mg sinking timescale ratio, which is close to 1 for the most of the parameter space outside this temperature range but is higher within it (up to about 2). In other words, while the relevant effect of thermohaline mixing is to erase differential sinking, for Si and Mg differential sinking is relatively weak at high and low temperatures anyway. This is why the mean metric value does not continue to increase for temperatures beyond about 16 000 K, even though thermohaline mixing itself is strongest at these high temperatures.

The overall strength of thermohaline mixing can be thought of as a combination of Figures 9 and 11. Figure 11 shows the potential impact of thermohaline mixing, while Figure 9 shows how likely such an impact is in the first place.

For the systems which might be affected by thermohaline mix-

ing, when thermohaline mixing is ignored, Fe and O are predicted to sink relatively quickly compared to major lithophile metals. For example, for a H-dominated white dwarf with $T_{\text{eff}} = 20000$ K and $\log(g) = 8$, STELUM predicts $\tau_{\text{Fe}} = 0.006$ yr and $\tau_{\text{O}} = 0.007$ yr, which is shorter than other key timescales (e.g., $\tau_{\text{Mg}} = 0.014$ yr, $\tau_{\text{Si}} = 0.012$ yr, $\tau_{\text{Ca}} = 0.008$ yr). Switching on thermohaline mixing erases the differences between these timescales, decreasing the inferred Fe and O content in the accreted material. Qualitatively, this results in the inference of more mantle-rich, less core-rich, less volatile-rich material.

In principle, the geology of accreted material could provide evidence either for or against it, if it were the case that one treatment consistently leads to more reasonable geological interpretations (with higher Bayesian evidence). We consistently find that the best geological model has higher Bayesian evidence, \mathcal{Z} , in the case where thermohaline mixing is neglected. The value of $|\Delta \ln(\mathcal{Z})|$ across all the entries we ran varies from 0.4 to 8.9, with a mean value of 4.8. In isolation, this would be equivalent to a Bayes factor of over 120. A caveat to this result is that the entries are not entirely independent of each other.

The underlying cause is that thermohaline mixing leads to inferences of higher accretion rates, and hence more massive pollutants (all else being equal). Our priors are weighted to penalise high mass pollutants, according to a collisional cascade size distribution. In other words, we assume that smaller pollutants are more plausible than larger ones (Cunningham et al. 2025), and since thermohaline mixing inherently demands larger pollutants, it is penalised. We emphasise that this result is driven by our assumptions rather than data. Nevertheless, it quantifies the intuition that the high accretion rates implied by thermohaline mixing are harder to explain dynamically. If one is confident that thermohaline mixing ought to be included, it would suggest that, broadly speaking, our assumed pollutant masses are too low, or that our assumed accretion events are too long.

6.2.1 Comparison against accretion rates derived from X-ray observations

The accretion rates inferred by our models may be tested against independently measured accretion rates determined via X-ray luminosity. At present, the only white dwarf with such a measurement is G 29-38, for which the accretion rate (expressed as $\log_{10} \text{g s}^{-1}$ throughout this section) is $9.21^{+0.25}_{-0.12}$ (Cunningham et al. 2022). G 29-38 is included in our sample, allowing for convenient comparison. We model this system with no overshoot (SN grid), with convective overshoot (S3D), and with both convective overshoot and thermohaline mixing. We adopt values of T_{eff} and $\log(g)$ from *Gaia*. The resulting accretion rates are $9.0^{+0.4}_{-0.3}$, $9.4^{+0.3}_{-0.4}$ and $11.8^{+0.3}_{-0.3}$ respectively. The values obtained without thermohaline mixing are consistent with the X-ray measurements, given the quoted uncertainties, as illustrated in Figure 12. The accretion rate obtained with thermohaline mixing is nominally inconsistent with the X-ray detections (at a significance level of 6.6σ). However, the X-ray constraint does not account for undetected emission, primarily in the UV. Including this additional contribution increases the inferred accretion rate, such that it may still be consistent with the estimate from thermohaline mixing (see dashed line in Figure 12).

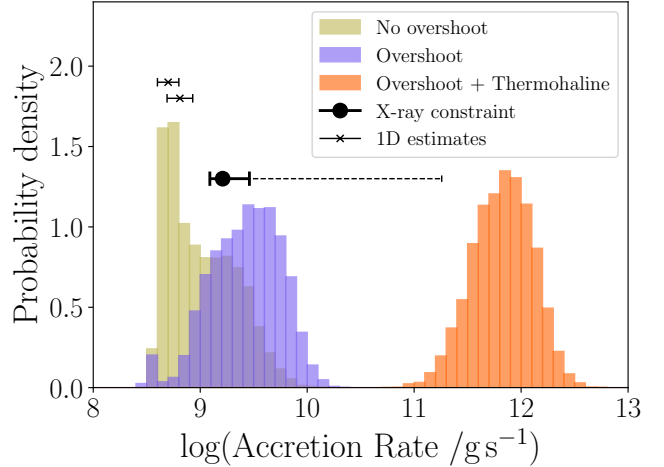


Figure 12. The accretion rate inferred for G 29-38 by our Bayesian framework using three sets of modelling assumptions: no convective overshoot (olive), convective overshoot (purple), convective overshoot plus thermohaline mixing (orange). The distributions are generated by randomly resampling 10,000 times from the posterior distributions associated with the best model in each case. For comparison, the black circle shows the value determined from X-ray detections by Cunningham et al. (2022), and the associated 1σ confidence interval. This value may be an underestimate, since it does not account for additional undetected emission, primarily in the extreme ultraviolet. The dashed line extending from the data point indicates the (90% confidence) upper limit on the estimated total accretion rate. We also show, for illustrative purposes only, previously published accretion rates estimated using 1D models (upper: Farihi et al. 2009, lower: Xu et al. 2014). The vertical positions of these points are arbitrary.

7 COMPARISON BETWEEN PUBLICLY AVAILABLE DIFFUSION TIMESCALES

This section, covering Tests 4 and 5, compares the publicly available Koester timescales grid ('KN') with a corresponding grid calculated with STELUM ('SN'). Convective overshoot is ignored in both cases in order to minimise the number of variables. The SN timescales can be considered to be equivalent to those that have been publicly available on the MWDD so far. As mentioned in Section 4.2, the Koester and STELUM frameworks make a few different assumptions, notably regarding the mixing-length parameter, the atmospheric boundary condition, and the heavy-element ionisation model. The comparisons performed in this section thus provide an estimate of the overall effect that these differences can have on the geological interpretation of accreted material.

Test 4 concerns H-dominated white dwarfs, while Test 5 covers He-dominated systems. We use our metric (Section 4.5) to select white dwarfs most likely to be affected by the differences between the KN and SN grid in both cases. For Test 4, our sample contains 17 entries (with 15 white dwarfs). The equivalent numbers for Test 5 are 25 and 19.

We illustrate the two samples in Figure 13 (H-dominated systems) and Figure 14 (He-dominated systems). These figures also repeat the methodology of Section 5.3 to show the regions of parameter space in which discrepancies between the STELUM and Koester timescales are most likely to be relevant. We discuss results for selected H-dominated systems in Section 7.1. He-dominated systems are discussed in Section 7.2 and Section 7.3 presents a broader overview.

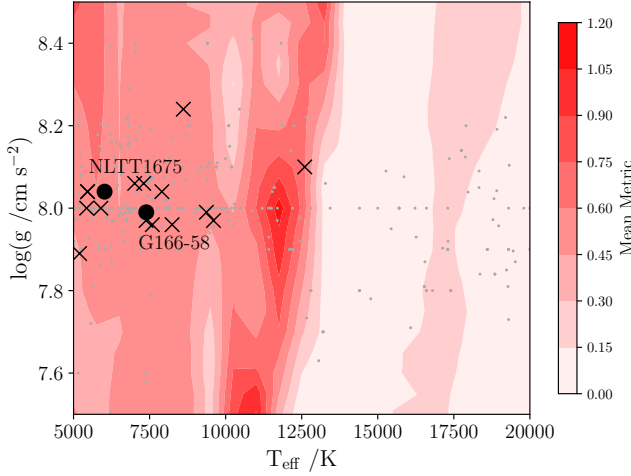


Figure 13. The susceptibility of H-dominated white dwarfs to a change in geological interpretation when switching between timescale grids SN and KN (i.e., using different modelling assumptions). The colour bar and label types are similar to those in Figure 5, but the black markers show the sample used for Test 4.

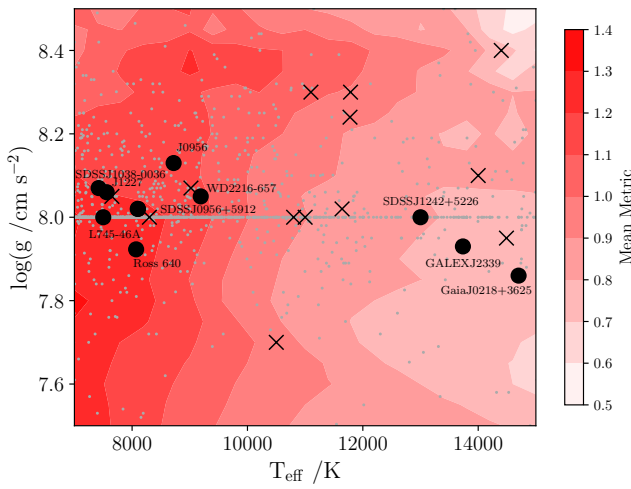


Figure 14. The susceptibility of He-dominated white dwarfs to a change in geological interpretation when switching between timescale grids SN and KN (i.e., using different modelling assumptions). The colour bar and label types are similar to those in Figure 5, but the black markers show the sample used for Test 5, and grey dots correspond to He-dominated white dwarfs.

7.1 H-dominated white dwarfs (Test 4)

For 2 of the 17 H-dominated entries we tested, we find that the favoured model changes when swapping between the SN and KN timescale grids. There were 3 entries which our code could not fit in any case (those associated with NLTT 7547). There were also 2 systems for which there was, nominally, a change in the favoured model, but at least one of the model fits was unphysical (WD J113444.64+610826.68 and WD 1455+298).

For NLTT 1675 (Kawka & Vennes 2012), incomplete condensation is invoked only when using the Koester grid (to 2.1σ). The key ratio is Ca/Mg. The detected Ca/Mg is slightly elevated relative to solar, but for the Koester grid, Ca sinks relatively fast in comparison to Mg. Therefore, the best model favours a pollutant composition with elevated Ca, which is achieved by condensation at high temperature.

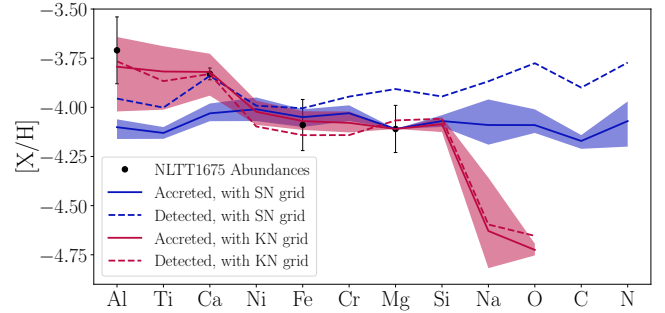


Figure 15. The geological interpretation of the metals accreted by NLTT1675 changes when switching between the STELUM (blue) and Koester (red) timescale grids, corresponding to different physical assumptions and treatments of the white dwarf physics. The plot features are similar to Figure 3. Our Bayesian framework finds evidence of incomplete condensation only when using the Koester grid.

The resulting composition is illustrated in Figure 15. The accreted material has previously been compared with CI chondrites by Kawka & Vennes (2012). Their results use timescales from Koester (2009), equivalent to an earlier version of our KN grid, and assume steady state accretion. For H-dominated white dwarfs it is often assumed that metal sinking timescales are sufficiently short, relative to the duration of an accretion event, that any other phase is highly unlikely to be observed. However, our results (with either timescale grid) favour a declining phase solution (with 94% confidence). NLTT 1675 is sufficiently cool that its metal sinking timescales are on the order of (at least) thousands of years. Our prior distribution for the accretion event duration goes down to 1 year, such that declining phase solutions are viable. In both cases, the median value of the accretion event duration was about 100 years (in units of log years, $2.4^{+1.8}_{-1.5}$ and $1.8^{+1.5}_{-1.2}$ for the SN and KN grids, respectively). The corresponding accretion rates (in units of $\log g s^{-1}$) are $10.6^{+1.6}_{-1.8}$ or $9.5^{+1.2}_{-1.5}$ respectively, and total accreted masses in the range of a small moon. These accretion rates fall within the range of values inferred for other white dwarfs (see Bauer & Bildsten 2018). Assuming a steady state solution, rather than declining phase, decreases the inferred Ca/Mg ratio of accreted material, bringing it closer to the chondritic value, because $\tau_{\text{Ca}} < \tau_{\text{Mg}}$.

For G 166-58, incomplete condensation is inferred (to 1.3σ significance) only for the SN grid. This is primarily driven by the change in Ni and Fe sinking times, which are (relatively) long for the SN grid, such that additional Ni and Fe depletion due to incomplete condensation is favoured, albeit marginally.

7.2 He-dominated white dwarfs (Test 5)

For 12/25 entries, there was no change in the overall interpretation, although this includes 3 entries for which our code could not fit the data (WD 1350-162, due to high Na, and both entries for HS 2253+8023).

There are 3 entries implying core-mantle differentiation when using the SN grid only (SDSS J124231.07+522626.6, SDSS J1038-0036 and J0956, to 4.7 , 3.6 and 2.4σ respectively). In all 3 cases, the accreted material is inferred to be mantle-rich. This can be understood as a consequence of the siderophile elements Ni and Fe sinking on (relatively) shorter timescales for the KN grid, such that depletions in these elements can be attributed to differential sinking. The magnitude of the timescale change is not large, but is

exacerbated by the inference that all three systems are in the declining phase of accretion.

Given this behaviour, it can be expected that the opposite outcome is possible: inference of core-rich material, but for the Koester timescales only. We indeed find an example of this outcome in WD 2216-657, to 1.8σ significance. However, in this case the interpretation is also dependent on the values of T_{eff} and $\log(g)$, with the inference of core-rich material occurring only with *Gaia* atmospheric parameter values (and Koester timescales).

For 6 entries (GALEXJ2339, WD 1425+540 (Model 1), L 745-46A, WD 1232+563 (Xu 2019), J1227 and Gaia J0218+3625), evidence for incomplete condensation is, nominally, ambiguous. For WD 1425+540, the change in favoured model is marginal (1.2σ) and can be attributed to random chance, and for WD 1232+563, our results are not trustworthy (see Section 5.2).

For the remaining 4 entries, unlike the case of differentiation, there is no consistent reason for the ambiguity. For L 745-46A, incomplete condensation is invoked with 2.7σ significance for the SN grid only. This is primarily due to the Fe sinking timescale, which is (relatively) longer when using the SN grid. This is roughly cancelled out by incomplete condensation, which slightly depletes Fe relative to the non-volatile rock forming metals. For GALEX2339 and J1227, incomplete condensation is invoked for the SN grid only (to 2.2σ and 1.7σ significance respectively) in order to match the abundance (or upper bound) of Na, a volatile metal. Na sinks (relatively) slowly for the SN grid, but not the KN grid, such that incomplete condensation is required to deplete it. Notably, GALEX2339 exhibits a high Be abundance. We do not model Be - if we did, it is unlikely that the geological processes we consider would be able to account for it. For Gaia J0218+3625 the key metal is O. For the Koester grid, O has a (relatively) long sinking timescale, such that additional heating is required to deplete it in this case only (to 2.3σ significance). In each of these four cases, except L 745-46A, the choice of T_{eff} and $\log(g)$ has an impact: the ambiguity noted above is only present for either the *Gaia* or PEWDD values, but not both. In other words, the presence of incomplete condensation depends not only on the timescale grid adopted, but also on the white dwarf parameter values.

There are three entries for which the presence of incomplete condensation and differentiation are both ambiguous. These are Ross 640 and both entries for SDSS J0956+5912, but note that these are practically identical.

For Ross 640, incomplete condensation is invoked when using the SN grid to 3.0σ . This appears to be driven by Ca, which sinks relatively slowly for SN (especially relative to Fe) such that the pollutant is inferred to be rich in Ca, implying thermal processing. This occurs when using white dwarf parameters from *Gaia*, which we consider marginally preferable in this case as the photometry avoids saturation. When using parameters from Blouin et al. (2018); Caron et al. (2023), differentiation is additionally invoked (to 1.4σ) for the SN grid only, for the reasons previously outlined.

For the two entries corresponding to white dwarf SDSS J0956+5912 which use data from Hollands et al. (2021), incomplete condensation and differentiation are both invoked to 4.3σ , only for the SN timescales. This is a combination of Ca sinking slower and siderophiles sinking faster for the KN grid.

7.3 Overview and discussion

Figure 13 shows the regions of parameter space in which discrepancies between the STELUM and Koester timescales are most likely to be relevant for H-dominated white dwarfs. The most affected region is a narrow band at around 12 000 K due to differences in the mixing-

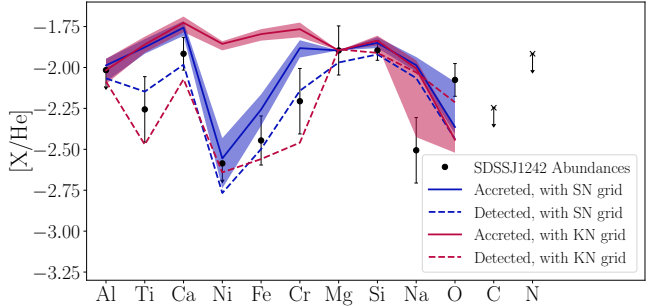


Figure 16. The geological interpretation of the metals accreted by SDSS J124231.07+522626.6 changes when switching between the SN (blue) and KN (red) timescale grids, corresponding to different physical assumptions and treatments of the white dwarf atmospheric physics. The plot features are similar to Figure 3. Our Bayesian framework finds (strong) evidence for accretion of mantle-rich material, and therefore core-mantle differentiation, only when using the SN grid. The data points for C and N are both upper bounds, and were both excluded when fitting the data because our incomplete condensation model does not accurately handle sub-Solar values for these elements. All four compositions shown here predict negligible quantities of C and N, so are consistent with the upper bounds.

length parameter. However, this part of parameter space is relatively sparsely populated. The white dwarfs we identified as having ambiguous geological interpretations have lower T_{eff} . This is because at lower temperatures, sinking timescales become longer, and declining phase solutions are viable. However, this is dependent on our prior distribution of accretion event duration. If the accretion event duration is assumed to always be at least 10^5 yr, it is likely that none of these systems would be affected by the choice of grid used here.

Figure 14 shows the equivalent for He-dominated white dwarfs. Here, the population of He-dominated white dwarfs (grey dots) is most concentrated in the most severely affected region of parameter space. The large difference seen at low temperature is likely due to the improved treatment of the boundary condition in the Koester code. However, this plot shows that the difference between the Koester and STELUM timescales can be relevant for almost any He-dominated white dwarf. Such systems are far more likely to be in the declining phase due to their long sinking timescales, exacerbating this issue. Therefore, the input physics appears to be the most important source of uncertainty for He-rich white dwarfs. In fact, the comparison presented here does not even tell the full story, as some modelling aspects are treated identically in the Koester and STELUM frameworks. For instance, both codes use the He equation of state of Saumon et al. (1995), which is highly uncertain in the regime of cool white dwarf envelopes and directly affects the depth of the convection zone (Koester & Kepler 2015). Both codes also handle diffusion using the screened Coulomb potential approximation of Paquette et al. (1986a), which breaks down in cool He-rich white dwarfs (Heinonen et al. 2020). More theoretical work on sinking timescales is clearly needed. In the meantime, our tests highlight that the Koester timescales tend to shift inferred pollutant compositions towards core-rich material and away from mantle-rich material, while the STELUM timescales have the opposite effect.

8 SYSTEMS WITH ROBUST INTERPRETATIONS

So far, we have focussed our attention on systems for which the interpretation of accreted material depends on the treatment of the white dwarf itself. It is also important to point out that there are

are systems whose geological interpretation does not change, and so appears to be qualitatively robust. This can occur when certain metals are so strongly enhanced or depleted (relative to uncertainties) that a certain geological interpretation is inevitable, regardless of the sinking timescales used. We describe the four most statistically significant examples of such systems, drawn from the samples investigated in this work. These are WDJ 183352+321757, HE 0106–3253, PG 1225–079 and GD 133. To confirm that our conclusions for these systems are robust, we have rerun our code using all relevant combinations of timescale grids¹⁰, white dwarf parameters, and inclusion/exclusion of thermohaline mixing. We illustrate an example of our model fits to the data for each of these systems in Figure 17.

Our metric predicts that WDJ 183352+321757 should be highly sensitive to the choice of STELUM or Koester timescale grids. In practice, its atmosphere is so strongly enriched in Fe and Ni that a core–mantle differentiation is always reached regardless, with very high confidence ($>30\sigma$). We also consistently find strong evidence for incomplete condensation ($>10\sigma$). The overall interpretation, which is qualitatively consistent in all cases, is that the accreted material originated in a parent body which formed at high temperature (with a median temperature between 1570 K and 1580 K in all cases), and which differentiated into a core and mantle in Earth-like proportions – the molar core fraction is close to 0.16 in all cases, close to an Earth-like value of roughly 0.17 (McDonough 2003). The accreted material itself was predominantly core-like, with a molar core fraction ranging between 0.59 and 0.60. We also find that accretion has likely reached the declining phase, with probability $> 99.6\%$.

Similarly, we find that for HE 0106–3253, our results show strong evidence for both incomplete condensation and core–mantle differentiation, due to its relatively high Ca and Fe abundances respectively. The confidence level for incomplete condensation ranges from $7.8\sigma – 9.4\sigma$, with the equivalent range for differentiation being $7.8\sigma – 9.6\sigma$. In all cases, we find that this white dwarf has accreted core-rich material (with molar core fraction ranging from 0.49 to 0.64). We also infer that the parent body of the accreted material had a relatively low (molar) core fraction, with values ranging from 0.04 to 0.07. This is comparable to Mars, for which the equivalent value is approximately 0.08 (Yoshizaki & McDonough 2020).

Klein et al. (2011) and Xu et al. (2013) found that PG 1225–079 had likely accreted refractory-enriched (i.e., volatile depleted) material. We find that this conclusion is robust. In all cases, and for all sets of abundances and parameters from both of these papers, incomplete condensation is confidently inferred (to $> 8\sigma$). This is driven by the relatively high abundances of the refractory metals Ti and Ca. The inferred condensation temperature is between 1390 K and 1500 K in all cases. We do not include the Sc, V and Mn detections or C, Be, S, Zn and Sr upper bounds in our modelling, but these do not obviously contradict our conclusion. We also consistently find a high ($> 96\%$) probability that accretion has reached the declining phase.

GD 133 exhibits a depletion of O, as well as a slight enrichment in the refractory element Ca, relative to Solar. Our framework robustly interprets this as evidence of incomplete condensation for every combination of parameters, with significance varying between 5.4 and 6.1σ . The associated temperature is consistently inferred to be high, with a median value between 1410 K and 1520 K.

We emphasise that these results, and in particular the extremely high confidence levels assigned to them in some cases, are dependent on the geological forward models within our Bayesian framework. Beyond a certain confidence level, the specific values are not very

meaningful because the ‘weak link’ is the model itself. Regardless, the key point we make here is that these results appear to be robust against the systematics under consideration in this paper. We also note that our samples were intentionally drawn from those regions of parameter space which are least conducive to robust results. Outside of these regions, we expect that there should be a greater proportion of systems with robust interpretations, all else being equal.

9 SUMMARY AND CONCLUSIONS

We have shown that the assumptions made about white dwarf physics can affect the geological conclusions drawn from material accreted by white dwarfs. This is because those assumptions affect the relative sinking timescales of different metals, which propagate into the inferred composition of the accreted material. We introduced a metric to quantify the discrepancy between two grids of sinking timescales as a function of T_{eff} and $\log(g)$. Our key findings are as follows.

Convective overshoot: For H-dominated white dwarfs, there is a sensitive regime between approximately 12 000 K and 18 000 K. In this zone, including a full 3D treatment of convective overshoot causes Fe and O to sink on (relatively) longer timescales compared to the no overshoot case. Including overshoot will, in general, decrease the inferred oxygen and iron content of accreted material. In borderline cases, neglecting overshoot can introduce spurious evidence of core-like material and/or an oxygen excess. We recommend using sinking timescales from the full 3D treatment of convective overshoot where possible, especially in this temperature range.

For He-dominated white dwarfs, the impact of convective overshoot is relatively minor, although this needs to be fully confirmed with 3D overshoot modelling. We show that, for most He-dominated white dwarfs (approximately speaking, those below about 16 000 K), ignoring convective overshoot is preferable to using overshoot fixed to 1 pressure scale height, as benchmarked against a variable treatment of overshoot.

Thermohaline mixing: The primary effect of thermohaline mixing is to increase the inferred accretion rate at H-dominated white dwarfs. The strength of this effect is primarily temperature-dependent, becoming stronger for hotter white dwarfs. For sufficiently high temperatures, thermohaline mixing becomes strong enough to disable differential sinking, potentially affecting geological interpretation. This is also dependent on the inferred accretion rate. The impact of thermohaline mixing on geology is to cause the inferred composition of accreted material to tend towards more mantle-rich/core-poor solutions, and also towards more volatile-rich solutions. While thermohaline mixing is expected to be important for H-dominated white dwarfs, the larger accretion rates implied by thermohaline mixing may be harder to explain dynamically. We have quantified this expectation in terms of Bayesian evidence, finding a mean improvement in $\ln(\mathcal{Z})$ of 4.8 when neglecting thermohaline mixing. We also find that the increased accretion rate inferred for G 29–38 is harder to reconcile with X-ray measurements.

Other physical assumptions: For He-dominated white dwarfs, differences in input physics (as captured by differences between STELUM and Koester sinking timescales) are potentially important across the full range of parameter space we tested, especially below about 10 000 K where the Koester code uses detailed boundary conditions. However, the sensitive regime is not clearly defined because the long sinking timescales associated with He-dominated atmospheres mean that any such white dwarf could plausibly be in the declining phase of accretion, which exacerbates the effects of timescale discrepancies. The clearest impact is that the Koester

¹⁰ Specifically, the KN, KF, and S3D/SV grids.

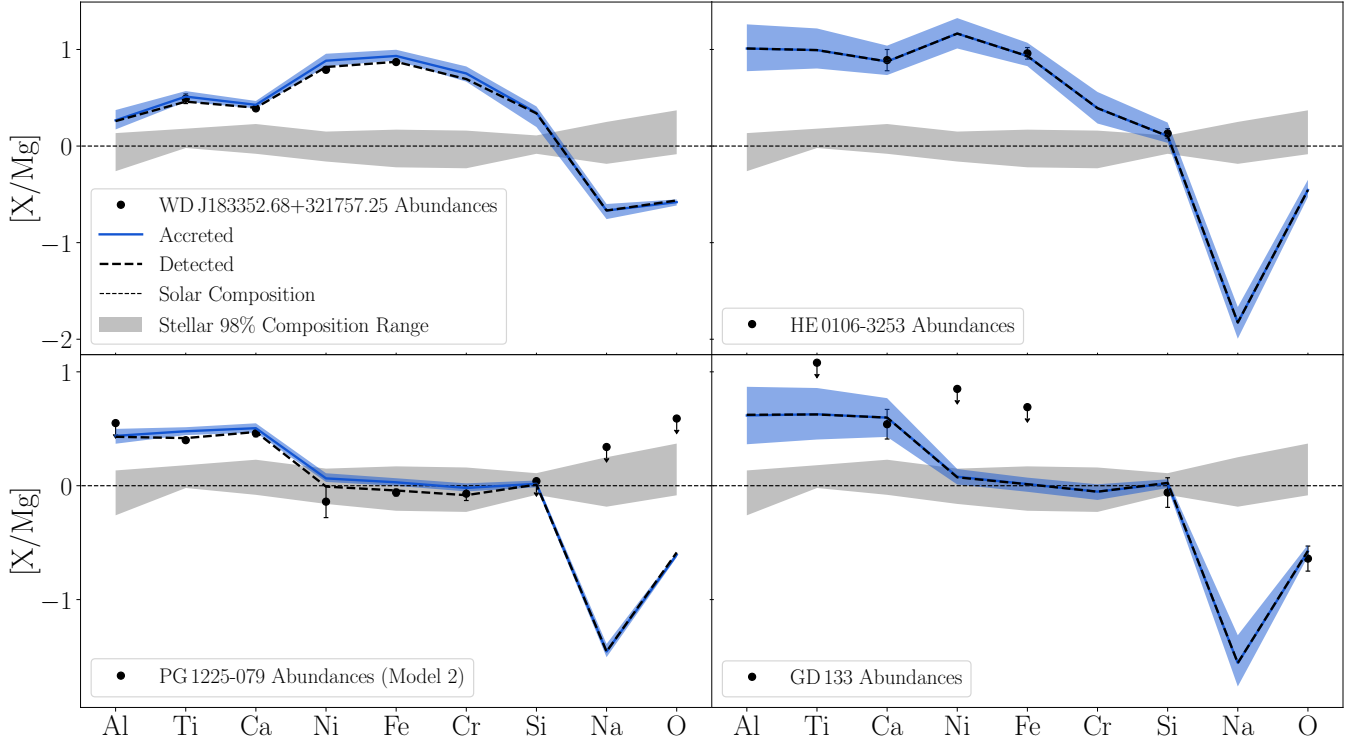


Figure 17. Representative model fits to the abundance data for four systems whose geological interpretation is robust against changes in white dwarf parameter values, sinking timescale grids, and treatment of thermohaline mixing. The blue line shows the inferred (median) composition of the accreted material, along with a 1σ confidence interval. The dashed black line shows the resulting detected composition, after accounting for differential sinking, excluding a confidence interval for visual clarity. The dashed black line may be compared against the data. For WD J183352+321757 and PG 1225-079, the example fit shown here uses the KN grid, and for PG 1225-079 we adopt abundance values for the ‘Model 2’ entry. For HE 0106-3253 and GD 133 we use the S3D grid, and include thermohaline mixing. Because thermohaline mixing is inferred to be active, and because it disables differential sinking, the accreted and detected compositions are close to identical in these cases. In all cases we use white dwarf parameters from *Gaia*.

timescales generally tend towards core-rich/mantle-poor solutions compared to the STELUM timescales. Since both of these grids (or close approximations) are publicly available, we recommend that both options be considered, and any discrepancies in the resulting interpretation reported.

The systematic effects described above can be mitigated against by modelling systems multiple times, covering a range of possible assumptions. We performed this exercise and identified four systems which, in the context of our model, yield robust geological interpretations at a high level of confidence. Two systems, PG 1225-079 and GD 133, have accreted material which experienced incomplete condensation at high temperature (roughly 1400 K). Two other systems, WD J183352+321757 and HE 0106-3253, witnessed both incomplete condensation and core–mantle differentiation, followed by accretion of a core-rich fragment of the resulting material.

In the longer term, models of white dwarf pollution should introduce uncertainties on (relative) sinking timescales, and propagate these through the forward model. These uncertainties should capture the discrepancies which can plausibly be introduced by a change in white dwarf modelling assumptions, and any correlation between them. In many cases, these uncertainties will be small (relative to uncertainties on the abundances themselves). However, in cases where they are non-negligible, this strategy should ensure that any geological conclusions are robust.

Geological modelling can itself be used to investigate whether certain treatments of element transport processes are favoured. This would require a compositional model of the reservoir(s) of mate-

rial which pollute white dwarfs, and a model for the typical timing of accretion events. The distribution of detected metal abundances across a large population of white dwarfs could be predicted using different sets of sinking timescales, and tested against data from a representative real sample.

ACKNOWLEDGEMENTS

AMB was supported by a Leverhulme Trust Grant (ID RPG-2020-366). This research received funding from the European Research Council under the European Union’s Horizon 2020 research and innovation programme number 101002408 (MOS100PC). TC was supported by NASA through the NASA Hubble Fellowship grant HST-HF2-51527.001-A awarded by the Space Telescope Science Institute, which is operated by the Association of Universities for Research in Astronomy, Inc., for NASA, under contract NAS5-26555. The authors would like to acknowledge the University of Warwick Research Technology Platform SCRTP for assistance in the research described in this paper. We thank Amy Bonsor and Paula Izquierdo for useful discussions. We also thank the anonymous referee for their helpful feedback, which improved the quality of the manuscript.

DATA AVAILABILITY

The geological inference code used in this work is publicly available at <https://github.com/andrewmbuchan4/PyllutedWD>

Public. White dwarf data are publicly available at <https://github.com/jamietwilliams/PEWDD>. The S3D and SV sinking timescale grids may be found at <https://zenodo.org/records/17313701>. We plan to implement the SV grid on the MWDD in the near future to incorporate the effect of convective overshoot. Therefore, our comments on the SN and SV grids apply to the MWDD versions before and after this change, respectively. Other sinking timescales calculated in this work will be shared upon request.

REFERENCES

Badenas-Agusti M., Viaña J., Vanderburg A., Blouin S., Dufour P., Xu S., Sha L., 2024, *Monthly Notices of the Royal Astronomical Society*, 529, 1688

Bauer E. B., Bildsten L., 2018, *The Astrophysical Journal Letters*, 859, L19

Bauer E. B., Bildsten L., 2019, *The Astrophysical Journal*, 872, 96

Bédard A., 2024, *Ap&SS*, 369, 43

Bédard A., Brassard P., Bergeron P., Blouin S., 2022a, *ApJ*, 927, 128

Bédard A., Bergeron P., Brassard P., 2022b, *ApJ*, 930, 8

Bédard A., Bergeron P., Brassard P., 2023, *ApJ*, 946, 24

Blouin S., Dufour P., Allard N. F., 2018, *The Astrophysical Journal*, 863, 184

Böhm-Vitense E., 1958, *Z. Astrophys.*, 46, 108

Buchan A., 2023, PhD thesis, Apollo - University of Cambridge Repository, doi:10.17863/CAM.104327, <https://www.repository.cam.ac.uk/handle/1810/361540>

Buchan A. M., Bonsor A., Shorttle O., Wade J., Harrison J., Noack L., Koester D., 2022, *Monthly Notices of the Royal Astronomical Society*, 510, 3512

Buchan A. M., Bonsor A., Rogers L. K., Brouwers M. G., Shorttle O., Tremblay P.-E., 2024, *Monthly Notices of the Royal Astronomical Society*, 532, 2705

Caron A., Bergeron P., Blouin S., Leggett S. K., 2023, *MNRAS*, 519, 4529

Cresswell I. G., Fraser A. E., Bauer E. B., Anders E. H., Brown B. P., 2025, *The Astrophysical Journal Letters*, 986, L10

Cukanovaite E., Tremblay P. E., Freytag B., Ludwig H. G., Fontaine G., Brassard P., Toloza O., Koester D., 2019, *MNRAS*, 490, 1010

Cukanovaite E., Tremblay P.-E., Bergeron P., Freytag B., Ludwig H.-G., Steffen M., 2021, *Monthly Notices of the Royal Astronomical Society*, 501, 5274

Cunningham T., Tremblay P.-E., Freytag B., Ludwig H.-G., Koester D., 2019, *Monthly Notices of the Royal Astronomical Society*, 488, 2503

Cunningham T., et al., 2021, *Monthly Notices of the Royal Astronomical Society*, 503, 1646

Cunningham T., Wheatley P. J., Tremblay P.-E., Gänsicke B. T., King G. W., Toloza O., Veras D., 2022, *Nature*, 602, 219

Cunningham T., et al., 2025, *Monthly Notices of the Royal Astronomical Society*, 539, 2021

Deal M., Deheuvels S., Vauclair G., Vauclair S., Wachlin F. C., 2013, *A&A*, 557, L12

Dohnanyi J. S., 1969, *J. Geophys. Res.*, 74, 2531

Doyle A. E., et al., 2023, *The Astrophysical Journal*, 950, 93

Dufour P., Blouin S., Couto S., Fortin-Archambault M., Thibeault C., Bergeron P., Fontaine G., 2017, in Tremblay P. E., Gänsicke B., Marsh T., eds, *Astronomical Society of the Pacific Conference Series Vol. 509, 20th European White Dwarf Workshop*. p. 3 ([arXiv:1610.00986](https://arxiv.org/abs/1610.00986))

Dupuis J., Fontaine G., Pelletier C., Wesemael F., 1992, *ApJS*, 82, 505

Elms S. A. K., et al., 2024, *MNRAS*, 534, 2758

Farihi J., Jura M., Zuckerman B., 2009, *The Astrophysical Journal*, 694, 805

Farihi J., Brinkworth C. S., Gänsicke B. T., Marsh T. R., Girven J., Hoard D. W., Klein B., Koester D., 2011, *The Astrophysical Journal*, 728, L8

Farihi J., Gänsicke B. T., Koester D., 2013, *Science*, 342, 218

Feynman R. P., Metropolis N., Teller E., 1949, *Physical Review*, 75, 1561

Fontaine G., Brassard P., Bergeron P., 2001, *PASP*, 113, 409

Fontaine G., Brassard P., Dufour P., Tremblay P. E., 2015a, in Dufour P., Bergeron P., Fontaine G., eds, *Astronomical Society of the Pacific Conference Series Vol. 493, 19th European Workshop on White Dwarfs*. p. 113

Fontaine G., Dufour P., Chayer P., Dupuis J., Brassard P., 2015b, in Dufour P., Bergeron P., Fontaine G., eds, *Astronomical Society of the Pacific Conference Series Vol. 493, 19th European Workshop on White Dwarfs*. p. 117

Freytag B., Ludwig H. G., Steffen M., 1996, *A&A*, 313, 497

Gaia Collaboration et al., 2023, *A&A*, 674, A1

Gentile Fusillo N. P., Gänsicke B. T., Farihi J., Koester D., Schreiber M. R., Pala A. F., 2017, *Monthly Notices of the Royal Astronomical Society*, 468, 971

Gentile Fusillo N. P., et al., 2021, *Monthly Notices of the Royal Astronomical Society*, 508, 3877

Gänsicke B. T., Koester D., Farihi J., Girven J., Parsons S. G., Breedt E., 2012, *Monthly Notices of the Royal Astronomical Society*, 424, 333

Harrison J. H., Bonsor A., Madhusudhan N., 2018, *Monthly Notices of the Royal Astronomical Society*, 479, 3814

Harrison J. H. D., Bonsor A., Kama M., Buchan A. M., Blouin S., Koester D., 2021, *Monthly Notices of the Royal Astronomical Society*, 504, 2853–2867

Heinonen R. A., Saumon D., Daligault J., Starrett C. E., Baalrud S. D., Fontaine G., 2020, *ApJ*, 896, 2

Hollands M. A., Tremblay P.-E., Gänsicke B. T., Koester D., 2021, *Monthly Notices of the Royal Astronomical Society*, 511, 71

Hoskin M. J., et al., 2020, *Monthly Notices of the Royal Astronomical Society*, 499, 171

Hummer D. G., Mihalas D., 1988, *ApJ*, 331, 794

Iglesias C. A., Rogers F. J., 1996, *ApJ*, 464, 943

Izquierdo P., Toloza O., Gänsicke B. T., Rodríguez-Gil P., Farihi J., Koester D., Guo J., Redfield S., 2020, *Monthly Notices of the Royal Astronomical Society*, 501, 4276

Jura M., 2003, *The Astrophysical Journal*, 584, L91–L94

Jura M., Munoz M. P., Farihi J., Zuckerman B., 2009, *The Astrophysical Journal*, 699, 1473

Kawka A., Vennes S., 2012, *A&A*, 538, A13

Kawka A., Vennes S., Ferrario L., Paunzen E., 2019, *Monthly Notices of the Royal Astronomical Society*, 482, 5201

Kenyon S. J., Bromley B. C., 2017, *The Astrophysical Journal*, 844, 116

Klein B., Jura M., Koester D., Zuckerman B., 2011, *The Astrophysical Journal*, 741, 64

Klein B. L., Doyle A. E., Zuckerman B., Dufour P., Blouin S., Melis C., Weinberger A. J., Young E. D., 2021, *The Astrophysical Journal*, 914, 61

Koester D., 2009, *Astronomy & Astrophysics*, 498, 517–525

Koester D., 2010, *Mem. Soc. Astron. Italiana*, 81, 921

Koester D., Kepler S. O., 2015, *A&A*, 583, A86

Koester D., Wolff B., 2000, *A&A*, 357, 587

Koester D., Gänsicke B. T., Farihi J., 2014, *A&A*, 566, A34

Koester D., Kepler S. O., Irwin A. W., 2020, *A&A*, 635, A103

Kupka F., Zaussinger F., Montgomery M. H., 2018, *MNRAS*, 474, 4660

Limbach M. A., et al., 2024, *The Astrophysical Journal Letters*, 973, L11

McDonough W. F., 2003, *Treatise on Geochemistry*, 2–9, 547

Melis C., Dufour P., 2017, *The Astrophysical Journal*, 834, 1

O'Brien M. W., et al., 2023, *Monthly Notices of the Royal Astronomical Society*, 518, 3055

O'Brien M. W., Tremblay P.-E., Klein B. L., Melis C., Koester D., Buchan A. M., Veras D., Doyle A. E., 2025, *Monthly Notices of the Royal Astronomical Society*, 539, 171

Paquette C., Pelletier C., Fontaine G., Michaud G., 1986a, *ApJS*, 61, 177

Paquette C., Pelletier C., Fontaine G., Michaud G., 1986b, *ApJS*, 61, 197

Putirka K. D., Xu S., 2021, *Nature Communications*, 12, 6168

Raddi R., Gänsicke B. T., Koester D., Farihi J., Hermes J. J., Scaringi S., Breedt E., Girven J., 2015, *Monthly Notices of the Royal Astronomical Society*, 450, 2083

Rogers L. K., et al., 2024a, *Monthly Notices of the Royal Astronomical Society*, 527, 6038

Rogers L. K., et al., 2024b, *Monthly Notices of the Royal Astronomical Society*, 532, 3866

Saumon D., Chabrier G., van Horn H. M., 1995, *ApJS*, 99, 713

Stanton L. G., Murillo M. S., 2016, *Phys. Rev. E*, 93, 043203

Steele A., Debes J., Xu S., Yeh S., Dufour P., 2021, *The Astrophysical Journal*, 911, 25

Swan A., Farihi J., Koester D., Hollands M., Parsons S., Cauley P. W., Redfield S., Gänssicke B. T., 2019, *Monthly Notices of the Royal Astronomical Society*, 490, 202

Swan A., Farihi J., Melis C., Dufour P., Desch S. J., Koester D., Guo J., 2023, *Monthly Notices of the Royal Astronomical Society*, 526, 3815

Tassoul M., Fontaine G., Winget D. E., 1990, *ApJS*, 72, 335

Tremblay P.-E., Ludwig H.-G., Steffen M., Freytag B., 2013, *A&A*, 559, A104

Tremblay P.-E., et al., 2020, *Monthly Notices of the Royal Astronomical Society*, 497, 130

Vennes S., Kawka A., 2013, *The Astrophysical Journal*, 779, 70

Wachlin F. C., Vauclair G., Vauclair S., Althaus L. G., 2017, *A&A*, 601, A13

Wang H. S., Lineweaver C. H., Ireland T. R., 2019, *Icarus*, 328, 287

Williams J. T., Gänssicke B. T., Swan A., O'Brien M. W., Izquierdo P., Cutolo A.-M., Cunningham T., 2024, *A&A*, 691, A352

Wilson D. J., Gaensicke B. T., Koester D., Toloza O., Pala A. F., Breedt E., Parsons S. G., 2015, *Monthly Notices of the Royal Astronomical Society*, 451, 3237–3248

Wyatt M. C., Farihi J., Pringle J. E., Bonsor A., 2014, *Monthly Notices of the Royal Astronomical Society*, 439, 3371

Xu S., Jura M., Klein B., Koester D., Zuckerman B., 2013, *The Astrophysical Journal*, 766, 132

Xu S., Jura M., Koester D., Klein B., Zuckerman B., 2014, *The Astrophysical Journal*, 783, 79

Xu S., Zuckerman B., Dufour P., Young E. D., Klein B., Jura M., 2017, *The Astrophysical Journal*, 836, L7

Xu S., Dufour P., Klein B., Melis C., Monson N. N., Zuckerman B., Young E. D., Jura M. A., 2019, *The Astronomical Journal*, 158, 242

Yoshizaki T., McDonough W. F., 2020, *Geochimica et Cosmochimica Acta*, 273, 137

Zuckerman B., Koester D., Melis C., Hansen B. M., Jura M., 2007, *The Astrophysical Journal*, 671, 872

Zuckerman B., Koester D., Dufour P., Melis C., Klein B., Jura M., 2011, *The Astrophysical Journal*, 739, 101

APPENDIX

Sample selection metric

We wish to quantify the potential impact of switching to a new set of timescales on the interpretation of the metal abundances of a white dwarf. We derive a simple expression, which can be applied in a pre-processing phase of modelling, to estimate this impact in a quantitative way.

We start by considering the relative abundances of two metals, i and j , as they evolve over time. We assume that material accretes at a constant rate starting at time $t = 0$, for a time of length t_{event} before switching off. The (number) abundance ratio of i to j , which we label as R_{ij} , evolves as

$$R_{ij} = R_{ij}^0 \frac{\tau_i}{\tau_j} \exp\left(\frac{t}{\tau_j} - \frac{t}{\tau_i}\right) \frac{\left[\exp\left(\frac{t}{\tau_i}\right) - 1\right]}{\left[\exp\left(\frac{t}{\tau_j}\right) - 1\right]}, \quad (3)$$

where τ_X is the sinking timescale of element X and $t_l = \min(t, t_{\text{event}})$. As time increases, R_{ij} deviates further from its initial value in the pollutant, R_{ij}^0 . The greatest potential discrepancy that can be introduced by a change in sinking timescales occurs at late times, so we consider the late time behaviour (i.e., $t \geq t_{\text{event}}$). Taking log (base 10) of both sides (since abundances are typically given on a log scale), the late time form of equation 3 becomes

$$\log_{10}(R_{ij}) \approx \log_{10}\left(R_{ij}^0 \frac{\tau_i}{\tau_j}\right) + \frac{t}{\ln(10)} \left(\frac{1}{\tau_j} - \frac{1}{\tau_i}\right). \quad (4)$$

Substituting $t = \beta\tau_i$, this can be simplified to:

$$\log_{10}(R_{ij}) \approx \log_{10}\left(R_{ij}^0 \frac{\tau_i}{\tau_j}\right) + \frac{\beta}{\ln(10)} \left(\frac{\tau_i}{\tau_j} - 1\right) \quad (5)$$

where β represents how deep we are into the declining phase, and assuming that all relevant diffusion timescales are of a similar order of magnitude, it does not matter much which one we use as a reference (i.e., we approximate $\beta = t/\tau$ without specifying which element). Note that when $\beta = 0$, we recover the result that in the steady state phase of accretion, the ratio of i and j is modified according to the ratio of their sinking timescales. Equation 5 can be thought of as a steady state modification (first term) plus a modification associated with the declining phase (second term). Now consider the change in this ratio that would result from swapping to a new set of timescales, with the sets labelled as a and b . The difference, Δ , is

$$\Delta = \log_{10}\left(\frac{\tau_i^a \tau_j^b}{\tau_j^a \tau_i^b}\right) + \frac{\beta}{\ln(10)} \left(\frac{\tau_i^a}{\tau_j^a} - \frac{\tau_i^b}{\tau_j^b}\right). \quad (6)$$

Broadly speaking, this change is significant when its magnitude exceeds the observational error. We therefore define our metric for i, j as

$$M_{a,b}^{i,j} = \frac{\left|\log_{10}\left(\frac{\tau_i^a \tau_j^b}{\tau_j^a \tau_i^b}\right) + \frac{\beta}{\ln(10)} \left(\frac{\tau_i^a}{\tau_j^a} - \frac{\tau_i^b}{\tau_j^b}\right)\right|}{\sqrt{\sigma_i^2 + \sigma_j^2}} \quad (7)$$

where σ_X is the 1 sigma uncertainty associated with X . The geological interpretation can, in principle, be affected by any pair i, j . We therefore iterate over all possible pairs, giving our final metric:

$$M_{a,b} = \max_{i,j}(M_{a,b}^{i,j}), \quad (8)$$

for all $i, j \in E$ where E is the set of all modellable elements.

In order to use this metric, we must estimate β , the number of sinking timescales we are into the declining phase. We firstly consider that for white dwarfs with short sinking timescales (e.g., warm H-dominated white dwarfs), the probability of observation in the declining phase is very low, so $\beta \approx 0$. We calculate an *a priori* probability of observation in declining phase, p as:

$$p = \frac{n\tau}{t_{\text{event}} + n\tau}, \quad (9)$$

where n is the maximum number of sinking timescales into the declining phase for which pollution could plausibly be detected and τ is any relevant sinking timescale (assuming they are all of a similar order of magnitude). We assume $n = 5$ and $t_{\text{event}} = 100$ kyr. In practice, the purpose of p is to act as a switch, being close to 0 for white dwarfs with short sinking timescales and close to 1 for white dwarfs with long sinking timescales.

We next consider that for white dwarfs deep in the declining phase, metal abundances become strongly correlated with their sinking timescales. We calculate the Pearson correlation coefficient, c , between the (log) of metal abundances and the corresponding sinking timescales, for white dwarfs with at least 4 modellable elements. We scale β with c if $c > 0$ (otherwise we ignore it). Finally, we scale β by n in order to ensure that the maximum value of β is n . This gives

$$\beta = pn \max(0, c), \quad (10)$$

in which p and c are both functions of the set of timescales being considered, so we calculate them for both grids a and b and adopt their mean values.

Our metric satisfies $M_{a,b}^{i,j} = M_{a,b}^{j,i} = M_{b,a}^{i,j} = M_{a,a}^{i,j} = 0$. For warm H-dominated white dwarfs with $\tau \ll t_{\text{event}}$, p (and therefore

β) is negligible and the numerator of Equation 7 reduces to the more familiar steady state scaling. For white dwarfs deep into the declining phase, M increases, but only if there is a difference in the timescale ratios. The terms in the numerator of Equation 7 are always the same sign so the declining phase can only increase the discrepancy (this also motivates ignoring negative values of c).

Our metric, especially the estimation of β , is only an approximation, and should be thought of as a heuristic indicator of which white dwarfs are most likely to suffer from a change in the adopted grid of sinking timescales. A complete evaluation would need to account for the values of the abundances themselves. This could be achieved by running our full Bayesian framework, but would defeat the purpose of using a simple metric to narrow down the number of target white dwarfs.

Metric performance

Our discrepancy metric can be thought of as predicting the strength of the effect of switching from one set of sinking timescales to another, measured in units of sigma. Crudely, one might expect that whether a geological result is robust depends on whether the sigma significance of the result is greater than the discrepancy metric. We investigate whether this is actually the case by plotting all geological results, from all 5 tests (excluding duplicate entries), by their sigma significance and the associated discrepancy metric.

The results are shown in Figure A1. We label ambiguous results with red crosses. These are results which are not recovered when switching to the other timescale grid in question. Unambiguous results are shown with blue circles. If the discrepancy metric were perfect, there would be no ambiguous results for which the sigma significance is greater than the metric. This is not the case: there are results which the metric falsely predicts to be robust, mostly for metric values below 1.8. We find that, above this threshold, the performance is much stronger, with a prediction accuracy of 95%. In practical terms, suppose that a model finds evidence of a geological process with sigma significance σ , and one wishes to know whether it is robust to a change to another set of sinking timescales without rerunning the model. If the metric value associated with that change in timescale grid is M , then if $\sigma > M > 1.8$, one could be 95% confident that the result is robust. If $\sigma < M$, Figure A1 shows that the result is likely not robust. If $\sigma > M$, but $M < 1.8$, Figure A1 shows that the result might still be robust as long as σ is sufficiently large.

Timescale ratios

The behaviour described in Sections 5–7 is driven by changes in sinking timescale ratios under different assumptions. Figure A2 illustrates this underlying behaviour for each of the 5 test cases for all modellable elements. Here, we fix the value of $\log(g)$ to 8 since the primary dependence is on T_{eff} . The Fe/Mg line of the top left panel is a cross-section through Figure 1 at $\log(g) = 8$. The other panels can be loosely thought of as cross-sections through Figures 6, 11, 13 and 14. This is not an exact equivalence, since those figures take into account accretion phase and which elements are detected.

This paper has been typeset from a $\text{TeX}/\text{L}\ddot{\text{A}}\text{T}\text{E}\text{X}$ file prepared by the author.

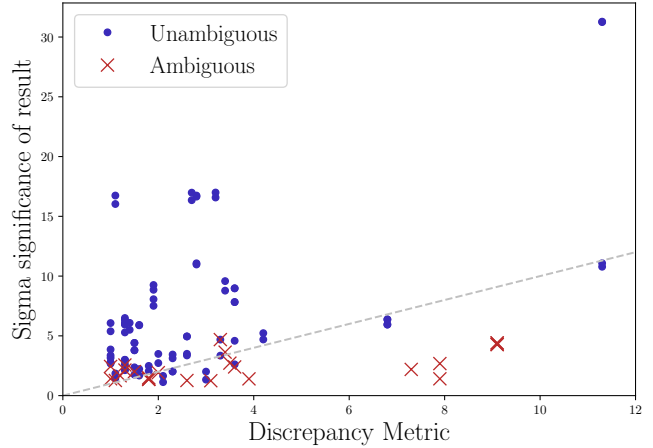


Figure A1. Performance of our discrepancy metric as a predictor for whether a result is ambiguous, i.e., can be lost when switching to a different timescale grid. If the metric was perfect, there would be no ambiguous results above the dashed line, which follows $y = x$. Some ambiguous results are above the dashed line: these are results which the metric falsely predicts to be robust. These false predictions are mostly limited to low metric values (below 1.8). For higher metric values, the performance is much stronger, with a prediction accuracy of 95%.

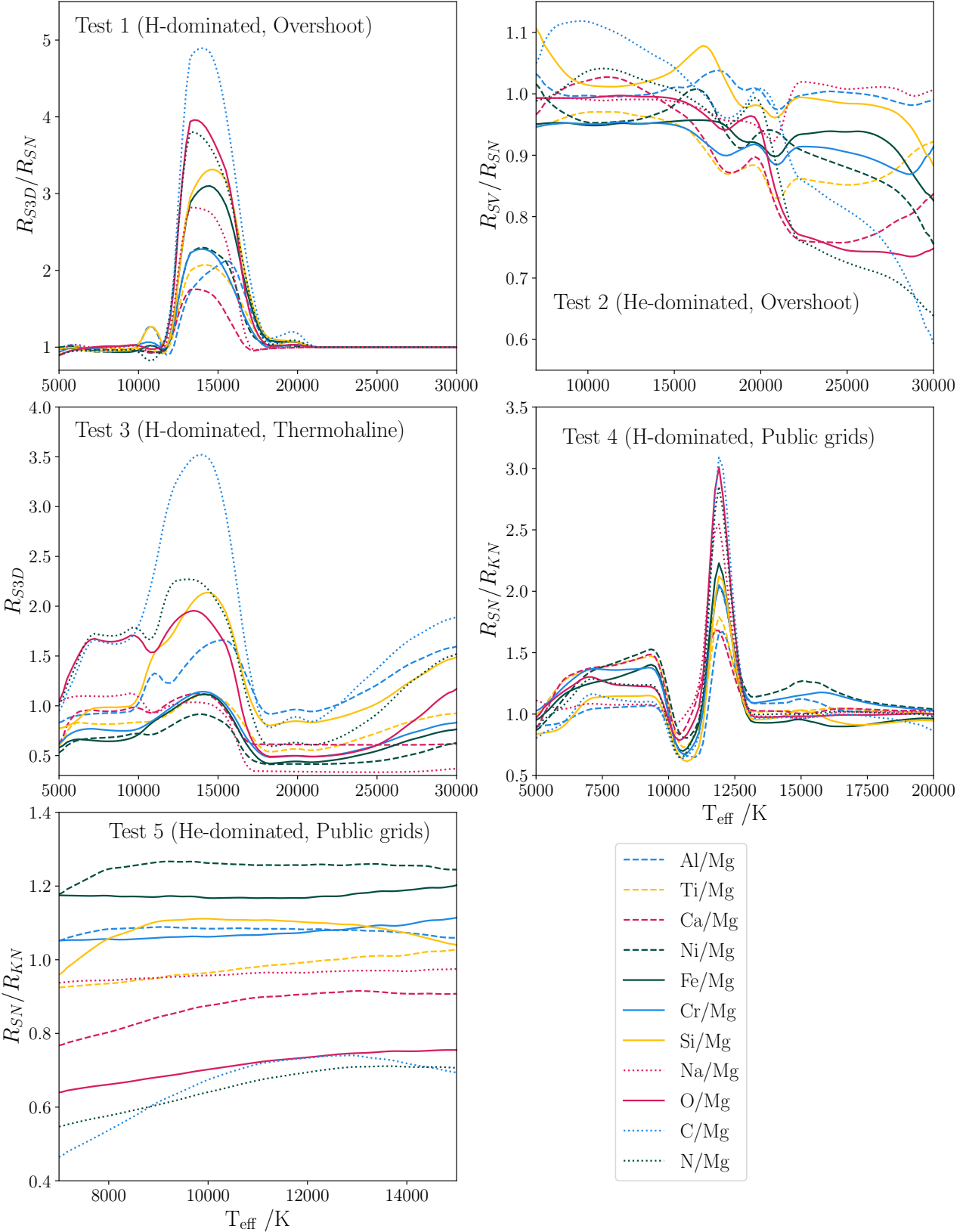


Figure A2. The dependence of key sinking timescale ratios on effective temperature, T_{eff} . Each panel shows the ratio of R as calculated using two different grids, labelled on the vertical axis. R denotes any of 11 sinking timescale ratios, indicated in the legend. For the panel labelled ‘Test 3’, the vertical axis is simply the value of R when using the S3D grid. For the panel labelled ‘Test 5’, the KN grid takes Ca/He as an additional variable. We set this to a (low) value of -15, to minimise the effect of this variable. We have smoothed the lines using a Savitzky-Golay filter to aid visual clarity.